Published in Energy Conversion and Management with doi: 10.1016/j.enconman.2025.120402

Optimizing Proton Exchange Membrane Electrolyzer Performance through dynamic pressure and temperature control: A Mixed-Integer Linear Programming approach

Roque Aguado[1], Marcos Tostado-Véliz[1,*], Umberto Desideri[2], Francisco Jurado[1]

1. Department of Electrical Engineering, University of Jaén, 23700 Linares, Spain (e-mail: ramolina@ujaen.es (R.A.), mtostado@ujaen.es (M.T-.V.), fjurado@ujaen.es (F.J.)).
2. Department of Energy, Systems, Territory and Construction Engineering, University of Pisa, Pisa 56122, Italy (e-mail: umberto.desideri@unipi.it)

* Correspondence: mtostado@ujaen.es

Abstract. Hydrogen is a key energy carrier for decarbonizing multiple sectors, particularly when produced via water electrolysis powered by renewable energy. Proton exchange membrane (PEM) electrolyzers are well suited for this application due to their ability to rapidly adjust to fluctuating power inputs. Despite being conventionally operated at high temperatures and pressures to reduce heating and compression needs, recent studies suggest that under partial loads, lower operating conditions may enhance efficiency. This study introduces a novel optimization framework for dynamically adjusting pressure and temperature in PEM electrolyzers. The model integrates an efficiency map within a Mixed-Integer Linear Programming (MILP) formulation and applies McCormick tightening to address nonlinearities. A one-week case study demonstrates operational cost reductions of up to 12.5% through optimal control, favoring lower temperatures and pressures at low current densities and higher temperatures near rated load, while maintaining moderate pressures. The results show improved efficiency and reduced hydrogen crossover, enhancing safety and enabling scalable application over extended time horizons. These insights are valuable for long-term planning and evaluation of hydrogen production and storage systems.

Keywords. Green hydrogen; MILP optimization; PEM electrolysis; Energy management.

Nomenclature

Electrochemical model	
U^{cell}	Cell voltage (V)
U^{act}	Activation overvoltage (V)
U^{ocv}	Open-circuit voltage (V)
U^{res}	Ohmic overvoltage (V)
T	Stack temperature (K)
p^c, p^a	Cathode, anode working pressure (Pa)
ΔG_T	Free Gibbs energy difference of the electrolysis at temperature T (J/mol)
Δh_T	Enthalpy difference of the electrolysis at temperature T (J/mol)
Δs_T	Entropy difference of the electrolysis at temperature T (J/mol·K)
$h_T^{x,p}$	Enthalpy difference of the substance x in phase p at temperature T with respect to the standard enthalpy (J/mol)
$s_T^{x,p}$	Entropy difference of the substance x in phase p at temperature T with respect to the standard entropy (J/mol·K)
R	Gas constant (J/mol·K)
α	Charge transfer coefficient (-)
z	Number of electrons (-)
F	Faraday constant (C/mol)
j	Current density (A/cm²)
j_0	Current exchange density (A/cm²)
j_0^{ref}	Reference current exchange density (A/cm²)
E_A	Activation energy (J/mol)
T^{ref}	Reference temperature (K)
R_0	Interface resistance (Ω·cm²)
d^m	Membrane thickness (cm)
δ^m	Membrane swelling factor (-)
σ^m	Membrane resistance (1/Ω·cm)
a^x	Activity of the substance x (-)
U^{tb}	Thermobalanced voltage (V)
U^{tn}	Thermoneutral voltage (V)
E^H	Energy required to heat water from 20°C to T (J/mol)
H_{ev}^{gas}	Evaporation energy of the water (J/mol)
$\dot{n}^{x,p}$	Molar flow rate of substance x in phase p (mol/s)
p^{sv}	Saturated vapor pressure (Pa)
S	Total cell active area (cm²)
Q^w, P^H	Waste heat rate, heating power (W)
$\dot{n}_d^{x,p}$	Molar diffusion flow rate of substance x in phase p (mol/s)
ϵ^x	Permeability of substance x (mol/cm·s·Pa)
Δf^x	Fugacity difference (Pa)
y^x	Molar fraction of substance x (-)
$\tilde{p}^c$, $\tilde{p}^a$	Partial cathode, anode pressure (Pa)
Υ	Proportionality factor (Pa·cm²/A)
r^C	Compression ratio (-)
p^{in}, p^{out}	Inlet, outlet pressure (Pa)
N	Number of compression stages (-)
P^C	Compression power (W)

γ	Isotropic coefficient (-)
η^C	Mechanical efficiency of compressor (pu)
T_n^{cooler}	Intercooler temperature in stage n (K)
η^F	Faraday efficiency (pu)
η	System efficiency (pu)
LHV^x	Lower heating value of substance x (J/mol)
Scheduling model	
P^{im}, P^{ex}	Power imported, exported with the grid (MW)
W^{im}, W^{ex}	Importing, exporting energy price (€/MWh)
u^{su}	Start-up status (binary)
c^{su}	Start-up costs (€)
P^{PV}	Photovoltaic generation (MW)
u^{sb}	Standby status (binary)
P^{sb}	Standby consumption (MW)
u^{Grid}	Importing/exporting status (binary)
$\overline{P}^{Grid}$	Importing/exporting cap (MW)
$\dot{m}^{PEM}$	Hydrogen generation (kg/h)
$\dot{m}^{S}$	Hydrogen directly supplied (kg/h)
$\dot{m}^{in}$, $\dot{m}^{out}$	Hydrogen storage inflow, outflow (kg/h)
$\dot{m}^{D}$	Total hydrogen supplied (kg/h)
m	Hydrogen demand (kg/h)
M	Total hydrogen stored (kg)
$\underline{M}$, $\overline{M}$	Minimum, maximum capacity of the storage system (kg)
u^S	Charging/discharging status (binary)
$\overline{m}^{in}$, $\overline{m}^{out}$	Inflow, outflow rate (kg/h)
u^{on}, u^{off}	Electrolyzer on, off status (binary)
$\underline{j}$, $\overline{j}$	Minimum, maximum current density (A/cm²)
Proposed solution strategy	
K	Number of current density maps evaluated (-)
w	Auxiliary variable to linearize the efficiency map (binary)
φ	Auxiliary variable representing the inverse of the efficiency (pu)
ψ	Auxiliary variable to linearize the product of current density and φ (A/cm²)
ω	Auxiliary variable to linearize the product of current density and η^F (A/cm²)
i	Iteration counter (-)
ζ, $\underline{\zeta}$	Contraction factor and its minimum value (pu)
tol	Convergence threshold (-)
κ	Auxiliary parameter (-)

1 – Introduction

1.1 – Context and motivation

The growing ambition to address climate change, as strongly reflected in the 2015 Paris Agreement and the European Green Deal, has significantly heightened the focus on hydrogen as a key energy carrier for the future energy transition [1]. Due to its versatility, hydrogen has the potential to contribute to the decarbonization of multiple sectors, including chemical production,

steelmaking, and shipping, among others [2]. Furthermore, hydrogen could serve as a storage medium for electricity generated from renewables, thus facilitating the massive penetration of renewable generators into the power system [3]. To ensure environmental sustainability through the widespread use of hydrogen, its production method needs to be carbon neutral. Currently, the overwhelming majority of hydrogen production is reliant on fossil fuels (predominantly, natural gas) [4], underscoring the urgent need to develop and promote clean hydrogen production technologies, such as water electrolysis powered by renewables.

1.2 – Water electrolysis technologies

Nowadays, alkaline electrolyzers represent the most mature technology for water electrolysis [5]. Alkaline technology features high efficiency and low investment costs [6]. However, proton exchange membrane (PEM) electrolyzers are recognized for their superior dynamic response, which allows them to adjust their operating conditions. This capability makes PEM electrolyzers particularly suitable for the integration of intermittent renewable energy sources, such as wind and solar power [7]. Thereby, PEM electrolyzers can be scheduled based on forecasted renewable generation or energy prices, enhancing their economic performance and efficiency. Accordingly, this work focuses on optimizing the operation of PEM electrolyzers in response to variable renewable energy generation and energy price fluctuations.

Alternative electrolysis technologies, such as Solid Oxide Electrolyzers (SOE) [8] and Anion Exchange Membrane Electrolyzers (AEME) [9], offer promising features and have the potential to address some of the limitations associated with conventional alkaline and PEM technologies. For instance, SOE units require less electrical energy for hydrogen production compared to PEM electrolyzers, owing to their ability to utilize thermal energy. However, they operate at elevated temperatures and typically require a high-temperature external heat source to maintain optimal conditions [10]. By contrast, AEMEs have the potential to produce hydrogen at lower costs, but their current performance is hindered by limited catalyst activity and low membrane conductivity [11]. Furthermore, both SOEs and AEMEs remain in the developmental stage and have yet to achieve widespread commercial deployment.

1.3 – Scheduling models for PEM electrolyzers

Most of the existing scheduling models for PEM electrolyzers rely on significant simplifications. These approaches typically consider the input power or hydrogen output as the sole control variable, thus resulting in a black-box model. The simplest models assume constant efficiency and a single operational state. Such approaches have been successfully applied to planning models [12] or integrated assessment tools [13], within different frameworks such as power systems [14], microgrids [15] or energy communities [16], among others. More sophisticated models, however, account for different operational states. For instance, a two-state operational model (on, off) is utilized in [17] to evaluate the techno-economic viability of electrolyzers providing grid services. Furthermore, three-state models (on, off, standby) have been used in [18] and [19] for planning and operational tools, respectively.

Other scheduling models assume a more realistic non-constant efficiency depending solely on the load level. Several approaches have been explored to model the characteristic non-constant efficiency of electrolyzers in scheduling tools. Pavić et al. [20] proposed a scheduling model for hybrid power plants integrating photovoltaic (PV) systems, batteries, and electrolysis, where the nonlinear electrolysis efficiency is linearized between two points using a single binary variable. In [21], nonlinear hydrogen production is linearized using piecewise functions, assessing the impact of the number of segments in the curve on the final results. Raheli et al. [22] suggested approximating the hydrogen production curve by quadratic interpolation, thus resulting in a second-order conic optimization model.

The models discussed above consider power input as single control variable for electrolysis scheduling. However, as with other technologies [23], the efficiency of PEM electrolysis is

affected by various operational parameters, namely power consumption, stack temperature, and working pressure [24]. While power-driven models can account for the effect of loading level on efficiency, they neglect the impact of temperature and pressure. Current commercial PEM electrolyzers allow working over a wide range of temperatures and pressures, enabling degrees of freedom to maximize the efficiency of electrolysis. In this regard, although several works demonstrate that the highest efficiency is typically achieved at low loading levels [25], the effect of temperature and pressure remains unclear, with some works suggesting that operating at low temperatures and pressures may be advantageous at low loading levels [26], thus contradicting theoretical foundations [27].

The effect of temperature has been considered in a number of works. Nevertheless, many of these studies assume fixed loading conditions [28-30], which limits the ability to dynamically adjust the working temperature for different loading levels. In [31], the nonlinear correlation between temperature and efficiency is approximated using tangent planes. However, this approximation relies on a reference point near the rated electrolyzer power. Although this approach may be valid for alkaline electrolyzers, it represents a questionable assumption when extended to PEM technologies. Baader et al. [32] approximated slow temperature dynamics in alkaline electrolyzers through piecewise functions, thus resulting in a Mixed-Integer-Linear Programming (MILP) model. Nonetheless, this approach focuses on the response of temperature to load variations rather than optimizing it to maximize the overall efficiency.

Unlike stack temperature, the effect of working pressure in electrolysis efficiency has been less extensively investigated. Valverde et al. [33] proposed a techno-economic model for microgrids including electrolysis, accounting for the effect of working pressure. Nevertheless, this approach considers pressure as an input parameter and, in consequence, its value is not optimized. Likewise, Hancke et al. [34] analyzed the impact of operating at high pressures (up to 180 bar) in PEM electrolyzers, demonstrating a general decrease in efficiency at higher pressures. However, this reference does not address the dynamic optimization of working pressure, treating it as an input parameter instead.

Whereas the references studied in this survey focus solely on the optimization of either power, temperature, or pressure, the combined optimization of these three parameters to achieve high efficiency has not yet been explored. In this regard, Bornemann et al. [26] represent a remarkable exception. This work proposes an optimization model for jointly optimizing the loading level, stack temperature, and working pressure of PEM electrolyzers. Nevertheless, the correlation between these parameters and the efficiency is modeled using nonlinear relationships, resulting in a nonlinear programming approach. Nonlinear optimization models require specialized solvers, which do not ensure the reachability of the global optimum within limited computational times [35]. Furthermore, nonlinear programming models face challenges in incorporating binary variables, thus limiting the consideration of electrolyzer operational states.

1.4 – Contributions and paper organization

This paper aims to develop an optimization model for scheduling power consumption, stack temperature, and working pressure in PEM electrolyzers, thereby enabling full versatility to maximize the overall efficiency of the electrolysis process. The proposed model seeks to address some of the limitations of the approach described in [26], offering two key advantages:

- The proposed model overcomes the nonlinear limitations inherent in the approach outlined in [26], which constrain its applicability and impede the integration of detailed operational representations. To address this, a novel Tightening-McCormick linearization strategy is employed, enabling the formulation of a highly accurate yet computationally efficient linear model. This approach captures the influence of loading level, stack temperature, and operating pressure within a MILP framework. As a result, globally optimal solutions can be obtained using standard optimization solvers, eliminating the need for specialized solution techniques. This enhances the model's portability and

facilitates its integration into broader optimization environments, such as long-term planning and energy system analysis tools.

- Owing to its linear structure, the proposed approach enables a straightforward representation of the operational states of PEM electrolyzers. Specifically, the three-state operational model presented in [21] is seamlessly integrated into the power-temperature-pressure optimization framework, resulting in a unified model capable of identifying efficient operating points while simultaneously generating realistic scheduling plans. In contrast to the nonlinear formulation in [26], which limits the incorporation of discrete operational modes, the linear MILP-based approach developed in this work allows the use of binary variables to represent state transitions in a computationally efficient and transparent manner.

In this context, and to the best of our knowledge, this study presents the first approach that simultaneously optimizes power, temperature, and pressure in PEM electrolyzers while explicitly incorporating operational states, all within a portable MILP framework. As such, the proposed model offers greater versatility and ease of implementation compared to prior approaches, such as that presented in [26], which rely on nonlinear formulations requiring dedicated solvers. By contrast, the linear formulation developed herein enables the use of widely available off-the-shelf solvers, making it more accessible and cost-effective from both computational and practical perspectives. This work thus contributes a valuable and adaptable computational tool that can be readily integrated into higher-level optimization platforms, such as energy system planning models, thereby facilitating more accurate and practical evaluations of PEM electrolyzer installations.

The new proposal is applied to a benchmark case study, where local hydrogen demand is supplied from a PEM electrolyzer, incorporating a PV system and hydrogen storage, as illustrated in Fig. 1. Several results are provided and discussed with the aim of validating the developed model and providing further insights on the effect of temperature and pressure on the efficiency of PEM electrolysis, thus complementing the conclusions in [26].

In the rest of the paper, Section 2 details the electrochemical model of PEM electrolyzers incorporating the effects of temperature and pressure. Section 3 outlines the scheduling model of the plant incorporating a PV system and hydrogen storage, along with the three-state operational model of the electrolyzer. Section 4 applies different linearization techniques in order to optimize power, temperature, and pressure employing a MILP model. Section 5 presents a case study with results. Finally, the main conclusions are duly drawn in Section 6.

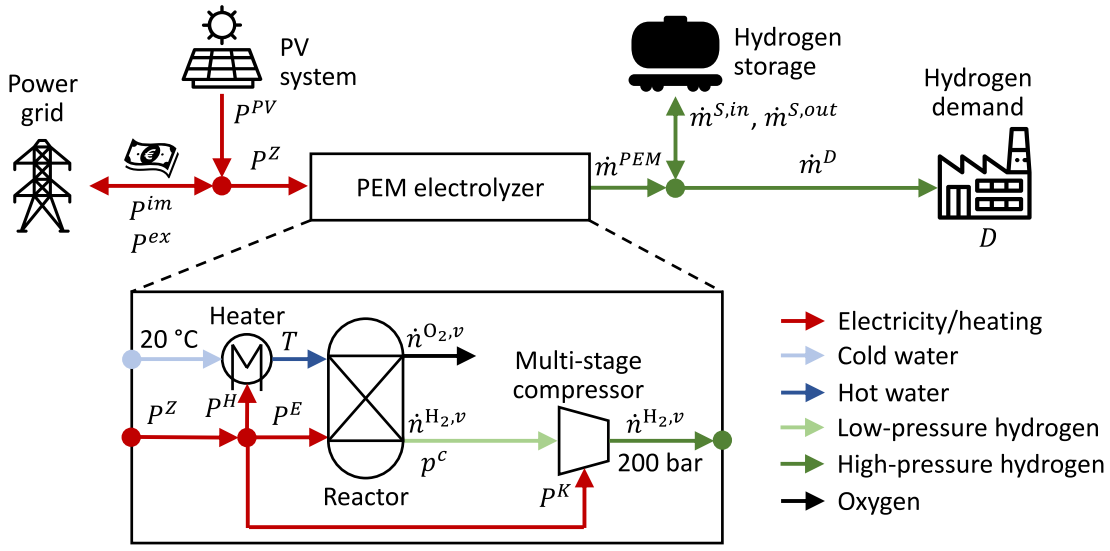

Fig. 1 – Schematic diagram of the benchmark case study incorporating PEM electrolysis and basic notation used throughout the paper. Time dependence is omitted in the figure for simplifying the notation.

2 – Electrochemical model

This section presents the electrochemical model of PEM electrolyzers, which is based on different well-known models documented in [25, 26, 36]. To simplify the notation, the dependence of time (i.e., t) is omitted throughout. For reproducibility, readers are referred to the data link in [26] and the IDAES manual [36], where the coefficients used in the model are provided. Furthermore, the particular data employed in this paper are reported in Section 5 and mostly align with those in the case study in [26].

As discussed later in the paper, the electrochemical model detailed in this section is based on well-established expressions that have been validated within the typical operational range of PEM electrolyzers. Accordingly, it is assumed that it can be applied to any commercial PEM electrolyzer without significant errors, provided that the operational temperature and pressure remain within 20 °C to 80 °C and up to 30 bar, respectively.

2.1 – Cell voltage

When the electrolysis reaction begins, current flows lead to an increment of the cell voltage above the open-circuit value. Overvoltages arise due to kinetic limitations and ohmic resistances within the cell. According to [26], diffusion overvoltages can be neglected as their impact is marginal for the current densities under consideration. Therefore, the total cell voltage can be expressed as the sum of the open-circuit voltage, and activation and ohmic overvoltages, as follows:

$$U^{cell} = U^{ocv} + U^{act} + U^{res} \tag{1}$$

The open-circuit voltage is calculated in (2) as a function of the free Gibbs energy, the number of electrons involved in the reaction, and the Faraday constant.

$$U^{ocv} = \frac{\Delta G_T}{zF} \tag{2}$$

The free Gibbs energy depends on the enthalpy and entropy differences of the electrolysis reaction, as well as on temperature, as follows:

$$\Delta G_T = \Delta h_T - T\Delta s_T \tag{3}$$

The enthalpy and entropy differences can be calculated as the partial differences of each substance with respect to the standard values. For example, the enthalpy difference Δh_T is calculated as in (4), while the entropy difference can be calculated using a similar approach.

$$\Delta h_T = H_T^{\mathrm{H_2},v} + 0.5H_T^{\mathrm{O_2},v} - H_T^{\mathrm{H_2O},l} \tag{4}$$

In this study, enthalpy and entropy differences relative to standard reference conditions are determined using established correlations fitted to experimental data. Specifically, molar-phase enthalpy and entropy values for gases are calculated using the formulations provided in [37], while thermodynamic properties for the liquid phase are derived from the expressions in [38]. It is important to highlight that these expressions are validated within specific temperature ranges: the gas-phase correlations for hydrogen and oxygen in [38] are applicable from −173.15 °C to 427 °C, and the liquid-phase correlations in [38] are valid between −1 °C and 280 °C. Given that the typical operating temperature range of PEM electrolyzers spans from 20 °C to 80 °C [26], the selected expressions are deemed appropriate and sufficiently accurate for the purposes of this work.

On the other hand, the activation overvoltage is given by an approximation of the Tafel equation in (5) [26].

$$U^{act} = \frac{RT}{\alpha zF}\ln\left(\frac{j}{j_0}\right) \tag{5}$$

In line with [26], the cathodic activation overvoltage is neglected and only the anodic activation overvoltage is considered. The temperature dependence of the current exchange density (j_0) can be established by the following relationship [39]:

$$j_0 = j_0^{ref} e^{\left(-\frac{E_A}{RT}\left(1-\frac{T}{T^{ref}}\right)\right)} \tag{6}$$

Lastly, the ohmic overvoltage depends on the current density and membrane parameters, as follows:

$$U^{res} = j\left(R_0 + \frac{d^m \delta^m}{\sigma^m}\right) \tag{7}$$

where the membrane resistance (σ^m) shows a nonlinear dependence with temperature, as shown in (8) [39].

$$\sigma^m = \left(0.6887 + a^{\mathrm{H_2O}}\right)^3 e^{\left(\frac{-10{,}440\left(a^{\mathrm{H_2O}}\right)^{0.25}}{RT}\right)} \tag{8}$$

2.2 – Heat management

During the electrolysis reaction, heat is generated internally due to overvoltages, while phase change from liquid water to gaseous hydrogen and oxygen results in cooling of the cell. Additionally, the inlet water needs to be pre-heated to reach the desired stack temperature. These processes require a heat management system that maintains the cell temperature within safe limits while controlling the temperature of the water flowing into the reactor. It is assumed that water is pre-heated by supplying heating power (P^H), while waste heat leaves the system boundary. The relationships between the heat generated internally, and the additional heat supplied to increase the water temperature, can be expressed via the thermobalanced voltage, which is given by [25]:

$$U^{tb} = U^{tn} + \frac{T\Delta s_T + E^H + H_{ev}^{gas}}{zF} \tag{9}$$

The thermoneutral voltage (U^{tn}) stands for the ideal voltage reaction, i.e., the cell voltage for which the reaction is thermally balanced [26]. The thermoneutral voltage can be calculated using the enthalpies of the species involved, as follows:

$$U^{tn} = \frac{\Delta H_T}{zF} \tag{10}$$

In (9), E^H corresponds to the energy that needs to be supplied to increase the water temperature through pre-heating. According to [26], E^H can be calculated as a function of the difference of enthalpies between the input and output of the heater, as expressed in (11).

$$E^H = \left(H_T^{\mathrm{H_2O},l} - H_{20°C}^{\mathrm{H_2O},l}\right) \cdot \left(1 + \frac{\dot{n}^{\mathrm{H_2O},v}}{\dot{n}^{\mathrm{H_2},v}}\right) \tag{11}$$

Note that inflow water is considered to be at 20 °C, as customary [25]. In (11), the amount of water vapor is calculated using (12), as a function of the total molar flow rate of hydrogen, the saturated vapor pressure and the anode and cathode working pressures [25]. It is assumed that the anode is at atmospheric pressure.

$$\dot{n}^{\mathrm{H_2O},v} = \dot{n}^{\mathrm{H_2},v}\left(\frac{p^{sv}}{p^c} + 0.5\frac{p^{sv}}{p^a}\right) \tag{12}$$

In (12), the saturated vapor pressure is calculated using the Antoine equation [37], which is valid over a wide range of temperatures, while the molar flow rate of hydrogen is calculated as explained later on. Finally, the enthalpy of water vaporization (H_{ev}^{gas}) is given by [25]:

$$H_{ev}^{gas} = T\Delta s_T\left(\frac{p^{sv}}{p^c} + 0.5\frac{p^{sv}}{p^a}\right) \tag{13}$$

If the cell voltage exceeds the thermobalanced one, waste heat is generated. Conversely, if the thermobalanced voltage is greater than the cell voltage, additional heat must be provided. With this in mind, the waste and supplied heat rates are derived using (14).

$$\begin{aligned} Q^w &= \left(U^{cell} - U^{tb}\right) jS, \text{if } U^{cell} > U^{tb} \\ P^H &= \left(U^{tb} - U^{cell}\right) jS, \text{if } U^{cell} < U^{tb} \end{aligned} \tag{14}$$

2.3 – Gas crossover

In PEM electrolyzers, gas transfer occurs due to the permeation of the membrane. Thereby, the permeated oxygen recombines with the hydrogen at the cathode, while a portion of the hydrogen permeates directly to the anode, leading to a loss of overall usable hydrogen. Hydrogen and oxygen diffusion can be calculated using the Fick's law, as follows:

$$\dot{n}_d^{x,v} = \epsilon^x S \frac{\Delta f^x}{d^m \delta^m}; x \in \{\mathrm{H_2}, \mathrm{O_2}\} \tag{15}$$

where the temperature-dependent permeabilities for each substance are defined by (16) [40].

$$\begin{aligned} \epsilon^{\mathrm{H_2}} &= 1.9 \cdot 10^{-17} e^{(0.0225/T)} \\ \epsilon^{\mathrm{O_2}} &= 3 \cdot 10^{-19} e^{(0.0191/T)} \end{aligned} \tag{16}$$

It is noteworthy that the expressions in (16) align with those used in [26] and are therefore considered suitable for the typical operational ranges of PEM electrolyzers. The total molar flow rate of hydrogen generated can be calculated as shown in (17), while (18) provides the amount of oxygen by-produced. Consequently, the molar fraction of each substance can be readily calculated as outlined in (19).

$$\dot{n}^{\mathrm{H_2},v} = \frac{jS}{zF} \tag{17}$$

$$\dot{n}^{\mathrm{O_2},v} = \frac{\dot{n}^{\mathrm{H_2},v}}{2} \tag{18}$$

$$y^x = \frac{\dot{n}^{x,v}}{\dot{n}^{\mathrm{H_2},v} + \dot{n}^{\mathrm{O_2},v}}; x \in \{\mathrm{H_2}, \mathrm{O_2}\} \tag{19}$$

The increase in partial pressures due to gas permeability needs to be taken into account. In line with [26], the cathode partial pressure is calculated using (20), which includes a proportional factor expressing the dependence with the current density (i.e., Υ).

$$\tilde{p}^c = y^{\mathrm{H_2}} p^c + \Upsilon j \tag{20}$$

Finally, the molar flow rate of hydrogen calculated in (17) is adjusted by considering the amount of hydrogen permeated to the anode and the amount of oxygen that recombines with hydrogen at the cathode, as follows:

$$\dot{n}^{\mathrm{H_2},v} = \dot{n}^{\mathrm{H_2},v} - \dot{n}_d^{\mathrm{H_2},v} - 2\dot{n}_d^{\mathrm{O_2},v} \tag{21}$$

2.4 – Compression

The hydrogen produced can either be supplied directly to the demand, or stored in high-pressure vessels. In line with [26], a 200 bar multi-stage compression system is considered in this paper. To minimize the overall compression work, a 5-stage compressor with intercooler and aftercooler is considered. The compression ratio is given by (22), while (23) calculates the total compression consumption [31]. Accordingly, the compression ratio per stage is limited to the range of 1.46 to 2.88, thereby keeping the temperature between stages within safe values.

$$r^C = \left(\frac{p^{out}}{p^c}\right)^{\frac{1}{N}} \tag{22}$$

$$P^C = \frac{R\dot{n}^{\mathrm{H_2},v}}{2(\gamma-1)\eta^C}\left(r^{C\left(\frac{\gamma-1}{\gamma}\right)} - 1\right) \cdot \left(T + \sum_{n=1}^{n=N-1} T_n^{cooler}\right) \tag{23}$$

2.5 – Efficiencies

The objective of the developed optimization model is maximizing the system efficiency, which is given by (24).

$$\eta = \frac{\dot{n}^{\mathrm{H}_2,v}\mathrm{LHV}^{\mathrm{H}_2}}{\underbrace{U^{cell}Sj+P^H+P^C}_{P^Z}} \tag{24}$$

As shown, the system efficiency establishes a ratio between the energy contained in the total hydrogen produced and the total system consumption (P^Z), accounting for electrical, heating and compression demands. The Faraday efficiency, as defined in (25), measures the gas crossover by relating the total and usable amounts of hydrogen.

$$\eta^F = \frac{\dot{n}^{\mathrm{H}_2,v}}{\dot{n}^{\mathrm{H}_2,v}+\dot{n}_d^{\mathrm{H}_2,v}+2\dot{n}_d^{\mathrm{O}_2,v}} \tag{25}$$

3 – Scheduling model

This section describes the scheduling model for the plant depicted in Fig. 1, consisting of a PV system, PEM electrolysis, and hydrogen storage. The operational strategy of the electrolyzer is formulated as a three-state model, according to [21]. Following this model, the electrolyzer can be operated in one of the three following states:

- On state: the electrolyzer operates within a valid range of current densities and produces hydrogen with a conversion efficiency, as in (24).
- Off state: the electrolyzer is disconnected, neither consuming power nor producing hydrogen. However, to switch back on, the electrolyzer requires a significant amount of energy, incurring in corresponding start-up costs.
- Standby state: the electrolyzer does not produce hydrogen, but consumes power to maintain internal temperature and pressure, being capable of transitioning from standby to on rapidly without incurring in start-up costs.

In line with [21], each state is represented by a binary variable, which indicates whether the electrolyzer is operated in that particular state. For instance, $u_t^{sb} = 1$ indicates that the electrolyzer is in standby mode at time t. The formulation presented in this section includes dependence on time (t), denoted as a subscript.

3.1 – Objective function

In this paper, the objective is to minimize the total energy cost over a predefined time horizon $\mathcal{T}$ (typically one week). For the plant under study, the total energy cost can be expressed, as follows:

$$Cost = \sum_{t\in\mathcal{T}}\left\{P_t^{im}W_t^{im} - P_t^{ex}W_t^{ex} + u_t^{su}c^{su}\right\} \tag{26}$$

The cost function (26) encompasses three terms. The first term represents the cost of imported energy from the upscale grid, priced under wholesale electricity prices (i.e., W^{im}). Wholesale prices are assumed to be dynamic, fluctuating hourly, as is common in wholesale electricity markets [41]. Nevertheless, other types of pricing mechanisms could be considered (e.g., flat tariffs). Likewise, the second term in (26) accounts for revenues from exporting energy, priced according to dynamic export rates (i.e., W^{ex}). The export price may be the same as the import price or different, though a discount factor is typically applied [42]. The last term is the start-up costs of the PEM electrolyzer, including the cost of switching on the electrolyzer [21].

3.2 – Power balance

In (27), the power balance of the plant is expressed, including the power exchanged with the main grid (both imports and exports), PV generation, and electrolyzer consumption. The last term

in (27) accounts for the standby consumption of the electrolyzer which typically ranges from 1–5% of the rated power [21].

$$P_t^{im} + P_t^{PV} - P_t^{ex} - \underbrace{\left(P_t^Z + u_t^{sb} P^{sb}\right)}_{\substack{Electrolyzer \\ consumption}} = 0; \forall t \in \mathcal{T} \tag{27}$$

It is worth noting that PV generation is highly dependent on weather conditions, which introduce inherent uncertainty into the model [43]. A detailed analysis of operational uncertainties lies beyond the scope of this work. Therefore, PV output is treated as a deterministic parameter, under the assumption that it can be forecasted with sufficient accuracy for the purposes of this study [44].

The total system consumption (P^Z) includes the power consumed for hydrogen production, as well as the power supplied for heating and compression. This power can be calculated as a function of the current density and system efficiency, as follows:

$$P_t^Z = 1.042 \cdot 10^{-6} \frac{j_t S \mathrm{LHV}^{\mathrm{H_2}}}{zF} \frac{1}{\eta_t}; \forall t \in \mathcal{T} \tag{28}$$

Note that (28) is given in MW to be consistent with the rest of the formulation and the system efficiency depends on the time, allowing it to vary for different load levels, temperatures, and pressures. Imports and exports are limited in (29) and (30), respectively. Moreover, an auxiliary binary variable is introduced to avoid unrealizable simultaneous imports and exports.

$$P_t^{im} \leq u_t^{Grid} \overline{P}^{Grid}; \forall t \in \mathcal{T} \tag{29}$$

$$P_t^{ex} \leq \left(1 - u_t^{Grid}\right) \overline{P}^{Grid}; \forall t \in \mathcal{T} \tag{30}$$

3.3 – Hydrogen generation and supply

When the electrolyzer is on, it consumes power to produce hydrogen. The instantaneous hydrogen mass flow can be calculated as a function of the current density and Faraday efficiency, as in (31).

$$\dot{m}_t^{PEM} = 7.2 \frac{j_t S}{zF} \eta_t^F; \forall t \in \mathcal{T} \tag{31}$$

Note that (31) is given in kg/h for consistency with the rest of the formulation. The hydrogen produced can either be supplied directly to the demand ($\dot{m}^s$) or stored in vessels ($\dot{m}^{in}$), as indicated in (32). On the other hand, the hydrogen demand can be met either directly from the electrolyzer or from the storage system ($\dot{m}^{out}$), as expressed in (33). Finally, the total hydrogen produced over the considered time horizon must be sufficient to completely satisfy local demand, as enforced by (34).

$$\dot{m}_t^{PEM} = \dot{m}_t^s + \dot{m}_t^{in}; \forall t \in \mathcal{T} \tag{32}$$

$$\dot{m}_t^D = \dot{m}_t^s + \dot{m}_t^{out}; \forall t \in \mathcal{T} \tag{33}$$

$$\dot{m}_t^D \geq D_t \tag{34}$$

3.4 – Hydrogen storage

The plant under consideration includes a hydrogen storage system equipped with vessels, where hydrogen can be stored at high pressure (200 bar). The instantaneous amount of hydrogen stored can be calculated as follows:

$$H_t = H_{t-1} + \dot{m}_t^{in} - \dot{m}_t^{out}; \forall t \in \mathcal{T} \backslash \{1\} \tag{35}$$

Since (35) is not defined at the beginning of the time horizon ($t = 1$), the initial hydrogen stored needs to be defined in (36), in alignment with [21]. To preserve consistency in the model, the amount of hydrogen stored at the end of the time window ($t = end$) is enforced to be the same as the initial amount in (37).

$$H_{(t=1)} = \underline{H} + \dot{m}^{in}_{(t=1)} - \dot{m}^{out}_{(t=1)} \quad (36)$$

$$H_{(t=end)} = H_{(t=1)} \quad (37)$$

Storage inflows and outflows are constrained by physical limits in (38) and (39), respectively. Similar to (29) and (30), auxiliary binary variables are included to avoid simultaneous charging and discharging of the storage system. Finally, the amount of hydrogen stored is limited by the actual capacity of vessels in (40), where a lower bound is also included, as suggested in some references [45].

$$\dot{m}^{in}_t \leq u^s_t \overline{m}^{in}; \forall t \in \mathcal{T} \quad (38)$$

$$\dot{m}^{out}_t \leq (1 - u^s_t) \overline{m}^{out}; \forall t \in \mathcal{T} \quad (39)$$

$$\underline{H} \leq H_t \leq \overline{H}; \forall t \in \mathcal{T} \quad (40)$$

3.5 – Operational states

According to the three-state operational model adopted, the electrolyzer can be in on, off, or standby states, but only one state can be active at any given time, as enforced by (41).

$$u^{on}_t + u^{off}_t + u^{sb}_t = 1; \forall t \in \mathcal{T} \quad (41)$$

Hydrogen is produced only when the electrolyzer is in the on state. In this state, power consumption falls within valid operational ranges, which is expressed in (42) by limiting the operational range of the current density. As seen, the binary variable u^{on} allows enforcing valid bounds for the current density. According to (42), current density can only be zero when the electrolyzer is in the off or standby states.

$$u^{on}_t \underline{j}_t \leq j_t \leq u^{on}_t \overline{j}_t; \forall t \in \mathcal{T} \quad (42)$$

An additional binary variable u^{su} is introduced to indicate the transition from off to on states. This binary variable allows accounting for start-up costs in (26) and must only activate when the electrolyzer switches back on from the off state. This logical coherence is ensured by (43), which prevents the activation of u^{su} when transitioning from standby to on. For consistency, it is assumed that the electrolyzer is not in the start-up state at the beginning of the time horizon, as enforced by (44). Furthermore, constraint (45) prevents the transition from off to standby states without first activating the start-up mode.

$$u^{su}_t \geq u^{on}_t - u^{on}_{t-1} - u^{sb}_{t-1}; \forall t \in \mathcal{T} \backslash \{1\} \quad (43)$$

$$u^{su}_{(t=1)} = 0 \quad (44)$$

$$u^{off}_{t-1} + u^{sb}_t \leq 1; \forall t \in \mathcal{T} \backslash \{1\} \quad (45)$$

3.6 – Optimal scheduling model

The optimal scheduling model for controlling power, pressure, and temperature in the plant under study reads as:

$$\min_{\Xi, p^c_t, T_t} \; Cost \quad (46a)$$

Subject to:

(27)-(45) (46b)

$$\eta_t, \eta^F_t = \Psi(j_t, p^c_t, T_t); \forall t \in \mathcal{T} \quad (46c)$$

$$u^{Grid}_t, u^s_t, u^{on}_t, u^{off}_t, u^{sb}_t, u^{su}_t \in \{0,1\}; \forall t \in \mathcal{T} \quad (46d)$$

where $\Xi = \left[P^{im}_t, P^{ex}_t, P^Z_t, j_t, \dot{m}_t, \dot{m}^s_t, \dot{m}^{in}_t, \dot{m}^{out}_t, \dot{m}^D_t, h_t, u^{Grid}_t, u^s_t, u^{on}_t, u^{off}_t, u^{sb}_t, u^{su}_t\right]$.

The model (46) minimizes the cost function in (46a), subject to the scheduling model described through Sections 3.2–3.5 in (46b). On the other hand, (46c) encapsulates the nonlinear

correlation of current density, working pressure, and stack temperature with the system and Faraday efficiencies, following the electrochemical model described in Section 2. Finally, binary variables are properly defined in (46d).

In present form, (46) is a Mixed-Integer Nonlinear Programming (MINLP) problem. Different approaches have been proposed in the literature for handling MINLP models, including outer approximation [46], heuristics [47], or decomposition techniques [48], among others. However, these methods often lack the reliability and efficiency of mature MILP solvers such as branch-and-bound algorithms [49]. Actually, the reachability of the global optimum in MINLP within a finite time is only guaranteed for convexifiable problems, which is not always possible [35]. This way, MILP models are typically preferred due to their portability (models can be easily implemented in different software and languages), reliability (global optimum reachability is guaranteed within a finite time) and efficiency. In the following section, a methodology to reformulate (46) as a MILP is proposed.

4 – The proposed linearization strategy

4.1 – Mapping the system efficiency

In (46), the system efficiency is computed as a nonlinear correlation depending on the current density, cathode pressure and stack temperature. According to the electrochemical model described in Section 2, there is a unique efficiency value for each tuple $\{j, p^c, T\}$. Let us assume that $k \in K$ different points are selected within valid ranges for each parameter in the tuple. Consequently, there is a unique value for both the system and Faraday efficiencies for each tuple, which can be calculated from the electrochemical model, as follows:

$$\eta_{k,k_1,k_2}, \eta^F_{k,k_1,k_2} = \Psi\left(j_k, p^c_{k_1}, T_{k_2}\right); \forall k, k_1, k_2 \in \{1,2,\dots,K\} \tag{47}$$

For simplicity in notation, it is assumed that all the parameters are evaluated at K different points, but this aspect can be adjusted for convenience. Expression (47) represents a mapping of system and Faraday efficiencies for the valid ranges of current densities, pressures and temperatures. Note that valid ranges for input parameters in (47) are typically available for each electrolyzer model, with typical values ranging from 1 to 30 bar and 20 to 80 °C [26]. Therefore, the map (47) can be easily computed offline and remains constant across all scheduling conditions.

For each current density, there is a unique value of maximum system efficiency, which can be easily derived from the map (47), as given by (48).

$$\overline{\eta}_k = \max_{k_1,k_2} \Psi\left(j_k, p^c_{k_1}, T_{k_2}\right); \forall k \in \{1,2,\dots,K\} \tag{48}$$

Hence, after running (47) and (48), a unique value of maximum efficiency is obtained for each current density. It allows formulating the system efficiency as a function of the current density, solely. However, optimal pressure and temperature for any current density can be inferred from the map (47), as follows:

$$p^c_k, T_k = \Psi^{-1}\left(\overline{\eta}_k\right); \forall k \in \{1,2,\dots,K\} \tag{49}$$

Note that (49) has a unique solution for each value of maximum efficiency, except for $j = 0$, where the system efficiency is zero for any working pressure and stack temperature. In such cases, if the electrolyzer is in standby, temperature and pressure remain at those values determined by operating conditions. By contrast, if the electrolyzer is shut down, both temperature and pressure drop to their minimum values. Nevertheless, temperature and pressure are computed *a posteriori*, after running the scheduling tool, and therefore, their values do not alter the solution of the mathematical model described in Section 3.

4.2 – Formulating the efficiency map as a MILP

After executing the map (48), K pairs of current densities and maximum efficiencies are obtained, allowing for a direct correspondence between j_k and $\overline{\eta}_k; \forall k$. Nonetheless, not all the possible current densities can be mapped, and therefore a direct correspondence of any arbitrary current density and efficiencies may not be available. To address this issue, the range of current densities is divided into $K-1$ sectors, with the k^{th} sector delimited by $[j_k, j_{k+1}]$. As a result, any current density value will fall within a specific sector, which is activated accordingly, then, a unique value of maximum system efficiency is assigned based on the activated sector. This approach ensures that every possible current density corresponds to a value of efficiency. The assigned maximum efficiency could either be the upper or lower bound of the activated sector, depending on the adopted scheduling strategy. However, assigning the lower bound is typically more conservative. To minimize potential errors, a sufficiently large value of K should be selected. For clarity, this sectorization strategy is illustrated in Fig. 2.

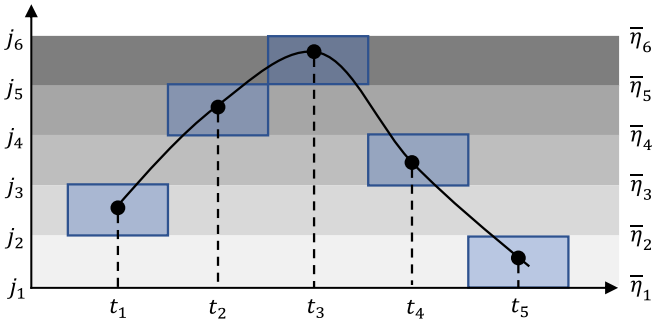

Fig. 2 – Illustration of the proposed sectorization strategy. The value of the instantaneous current density lies within one sector, which is activated (blue squares), assigning automatically a value of maximum system efficiency.

To integrate the proposed sectorization strategy into the scheduling tool (46), it must be formulated as a MILP. First, the auxiliary binary variable $w_{k,t}$ is introduced, which is equal to 1 if the k^{th} sector is activated at time t, and 0 otherwise. Thus, (50) enforces that j_t falls within the limits of the sector activated. On the other hand, (51) enforces that only one sector is activated at time t.

$$w_{k,t} j_k \leq j_t \leq w_{k,t} j_{k+1}; \forall k \in \{1,2,\dots,K-1\} \wedge t \in \mathcal{T} \tag{50}$$

$$\sum_k w_{k,t} \leq 1; \forall t \in \mathcal{T} \tag{51}$$

Since the system efficiency appears in a denominator in (28), it is useful to work with the inverse of the efficiency rather than the efficiency itself. Once a sector is activated, the inverse of the system efficiency can be derived from the mapping (48) using the dummy variable φ_t, whose value is given in (52). Similarly, the Faraday efficiency can be calculated using (53).

$$\varphi_t = \sum_k w_{k,t} \frac{1}{\overline{\eta}_k} \tag{52}$$

$$\eta_t^F = \sum_k w_{k,t} \eta_k^F \tag{53}$$

The inclusion of the dummy variable in (52) reformulates (28), as follows:

$$P_t^Z = 1.042 \cdot 10^{-6} \frac{j_t S \mathrm{LHV}^{\mathrm{H_2}}}{zF} \varphi_t; \forall t \in \mathcal{T} \tag{54}$$

Albeit (50)–(53) allow calculating the system and Faraday efficiencies using a MILP formulation, nonlinearities persist in (31) and (54) due the product of efficiencies and current densities.

4.3 – McCormick envelopes

Bilinear terms in (31) and (54) arise due to the product of the current density by the Faraday and system efficiency, respectively. These three variables have well-defined physical bounds, and

as such, they can be represented as box-constrained variables. The product of two continuous variables with known bounds can be effectively linearized using McCormick envelopes [50]. This technique approximates the original bilinear term through the use of convex and concave planes, which restrict the feasible solution space. The application of the McCormick envelopes to the two bilinear terms in (54) and (31) reads as:

$$\begin{cases} \psi_t \geq \underline{\varphi} \cdot j_t + \varphi_t \cdot \underline{j} - \underline{\varphi} \cdot \underline{j}; \forall t \in \mathcal{T} \\ \psi_t \geq \overline{\varphi} \cdot j_t + \varphi_t \cdot \overline{j} - \overline{\varphi} \cdot \overline{j}; \forall t \in \mathcal{T} \\ \psi_t \leq \underline{\varphi} \cdot j_t + \varphi_t \cdot \overline{j} - \underline{\varphi} \cdot \overline{j}; \forall t \in \mathcal{T} \\ \psi_t \leq \overline{\varphi} \cdot j_t + \varphi_t \cdot \underline{j} - \overline{\varphi} \cdot \underline{j}; \forall t \in \mathcal{T} \\ 0 \leq \psi_t \leq \overline{\varphi} \cdot \overline{j}; \forall t \in \mathcal{T} \end{cases} \tag{55}$$

$$\begin{cases} \omega_t \geq \underline{\eta}^F \cdot j_t + \eta_t^F \cdot \underline{j} - \underline{\eta}^F \cdot \underline{j}; \forall t \in \mathcal{T} \\ \omega_t \geq \overline{\eta}^F \cdot j_t + \varphi_t \cdot \overline{j} - \overline{\eta}^F \cdot \overline{j}; \forall t \in \mathcal{T} \\ \omega_t \leq \underline{\varphi} \cdot j_t + \varphi_t \cdot \overline{j} - \underline{\eta}^F \cdot \overline{j}; \forall t \in \mathcal{T} \\ \omega_t \leq \overline{\eta}^F \cdot j_t + \varphi_t \cdot \underline{j} - \overline{\eta}^F \cdot \underline{j}; \forall t \in \mathcal{T} \\ 0 \leq \omega_t \leq \overline{\eta}^F \cdot \overline{j}; \forall t \in \mathcal{T} \end{cases} \tag{56}$$

Note that some terms in (55) and (56) can be omitted, as some bounds are equal to zero (e.g., $\underline{\eta}^F$). However, the generic formulation presented above allows adapting the developed methodology to any other case easily. Moreover, (55) and (56) are linear constraints and do not contribute to increase computational complexity of the model. In (55) and (56), the variables ψ and ω replace the original bilinear terms, $j\varphi$ and $j\eta^F$, respectively. Thus, original constraints (54) and (31) are replaced by (57) and (58), respectively.

$$P_t^Z = 1.042 \cdot 10^{-6} \frac{S \mathrm{LHV}^{\mathrm{H_2}}}{zF} \psi_t; \forall t \in \mathcal{T} \tag{57}$$

$$\dot{m}_t^{PEM} = 7.2 \frac{S}{zF} \omega_t; \forall t \in \mathcal{T} \tag{58}$$

4.4 – MILP problem

After applying the mapping and McCormick linearization in sections 4.2 and 4.3, respectively, the original scheduling problem (46) is reformulated as the following MILP.

$$\min_{\substack{\Xi, \varphi_t, \eta_t^F \\ w_{k,t}, \psi_t, \omega_t}} \; Cost \tag{59a}$$

Subject to:

(27), (29), (30), (32)–(45) – Original constraints (59b)
(50)–(53) – Linearized efficiency map (59c)
(57), (58) – Linearization of (28) and (31) (59d)
(55), (56) – McCormick envelopes (59e)
$u_t^{Grid}, u_t^s, u_t^{on}, u_t^{off}, u_t^{sb}, u_t^{su}, w_{k,t} \in \{0,1\}; \forall k \in \{1,2,\dots,K-1\} \wedge t \in \mathcal{T}$ (59f)

In (59), the objective is minimizing the operation cost, as in the original model. However, the decision-space expands to include the new variables φ, w, ψ and ω. On the other hand, (59b) encloses the original scheduling problem in Section 3, but excluding the nonlinear constraints (28) and (31), which are replaced by their linear counterparts (59d). (59c) represents the linearized efficiency map, as described in Section 4.2, whereas (59e) includes the McCormick envelopes. Lastly, (59f) properly declares binary variables.

4.5 – Tightening strategy

The McCormick envelopes offer a reliable approximation of bilinear terms when the range of the variables involved is not excessively wide. Otherwise, the concave and convex estimators may deviate significantly from the original function, thus providing inaccurate solutions. To address this issue, tightening strategies can be employed [51], which gradually refine the original bounds to more accurately approximate the original bilinear function. This methodology is broadly described in Fig. 3 using the bilinear term $j\varphi$ (further approximated by the auxiliary variable ψ) as an example, whose real value is denoted by the continuous black line in the figure. Initially, bounds, $\left[\underline{j}^{(0)}, \overline{j}^{(0)}\right]$ and $\left[\underline{\varphi}^{(0)}, \overline{\varphi}^{(0)}\right]$ define McCormick estimators, depicted as continuous red lines in Fig. 3. The initial estimate of the auxiliary variable (i.e., $\psi^{(0)}$) is given by the intersection point of either the upper or lower McCormick initial estimators.

In the next iteration, initial bounds are contracted using a preestablished contraction parameter, namely $\zeta > 0$, resulting in the updated bounds $\left[\underline{j}^{(1)}, \overline{j}^{(1)}\right]$ and $\left[\underline{\varphi}^{(1)}, \overline{\varphi}^{(1)}\right]$. As shown in the figure, the resulting McCormick envelopes (depicted as continuous green lines) enclose a reduced feasible region (green-shaded area), which more closely approximates the true bilinear relationship. This iterative process continues until the absolute difference between the bilinear term and its auxiliary approximation falls below a predefined tolerance $tol \in \mathbb{R}_+\backslash\{0\}$.

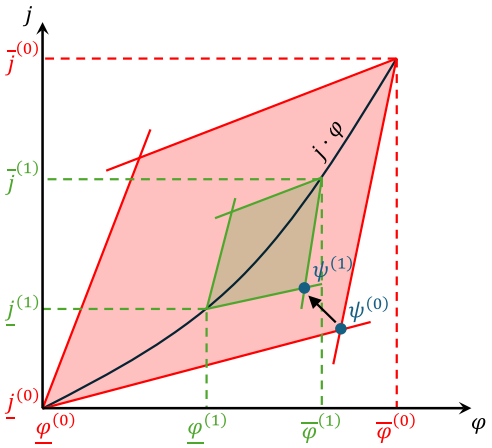

Fig. 3 – Illustration of the proposed McCormick tightening strategy.

The five-step methodology below describes the application of a tightening strategy to the problem under consideration.

- Step 0: set the iteration counter $i = 0$ and $\zeta, \underline{\zeta}, tol, \kappa \in \mathbb{R}_+\backslash\{0\}$. Set the original bounds for j, η and η^F according to physical limits. Set the bounds for φ and ω accordingly.
- Step 1: solve the problem (59) to obtain $j_t^{(i)}$, $\eta_t^{(i)}$, $\eta_t^{F,(i)}$, $\varphi_t^{(i)}$ and $\omega_t^{(i)}$.
- Step 2: calculate the error, as follows:

$$\varepsilon = \max\left(\frac{\left\| j_t^{(i)} \frac{1}{\eta_t^{(i)}} - \varphi_t^{(i)} \right\|_\infty}{\max_t \varphi_t^{(i)}}, \frac{\left\| j_t^{(i)} \eta_t^{F,(i)} - \omega_t^{(i)} \right\|_\infty}{\max_t \omega_t^{(i)}}\right) \tag{60}$$

- Step 3: if $\varepsilon \leq tol$, then stop. Else, update variable bounds, as follows:

$$\begin{cases} \underline{j}_t^{(i+1)} = \max\left((1-\zeta)\underline{j}_t^{(i)}, \underline{j}_t^{(0)}\right); \forall t \in \mathcal{T} \\ \overline{j}_t^{(i+1)} = \min\left((1+\zeta)\overline{j}_t^{(i)}, \overline{j}_t^{(0)}\right); \forall t \in \mathcal{T} \\ \underline{\varphi}_t^{(i+1)} = \max\left((1-\zeta)\underline{\varphi}_t^{(i)}, \underline{\varphi}_t^{(0)}\right); \forall t \in \mathcal{T} \\ \overline{\varphi}_t^{(i+1)} = \min\left((1+\zeta)\overline{\varphi}_t^{(i)}, \overline{\varphi}_t^{(0)}\right); \forall t \in \mathcal{T} \\ \underline{\omega}_t^{(i+1)} = \max\left((1-\zeta)\underline{\omega}_t^{(i)}, \underline{\omega}_t^{(0)}\right); \forall t \in \mathcal{T} \\ \overline{\omega}_t^{(i+1)} = \min\left((1+\zeta)\overline{\omega}_t^{(i)}, \overline{\omega}_t^{(0)}\right); \forall t \in \mathcal{T} \end{cases} \quad (61)$$

Go to Step 4.

- Step 4: update the iteration counter $i = i + 1$, and the contraction parameter, as follows:

$$\zeta = \max\left(\zeta - \kappa, \underline{\zeta}\right) \quad (62)$$

Go to step 1.

Formally, the convergence of the proposed algorithm is not guaranteed within a finite number of iterations. Consequently, it is necessary to impose an upper limit on the number of iterations, with the procedure deemed unsuccessful if convergence is not achieved within the specified threshold. Nevertheless, empirical results demonstrate that the proposed tightening strategy performs efficiently in practice, consistently converging within a small number of iterations across all tested scenarios.

4.6 – The developed methodology

The developed methodology for optimizing pressure and temperature in PEM electrolyzer scheduling tools using a MILP formulation is described in the flowchart of Fig. 4.

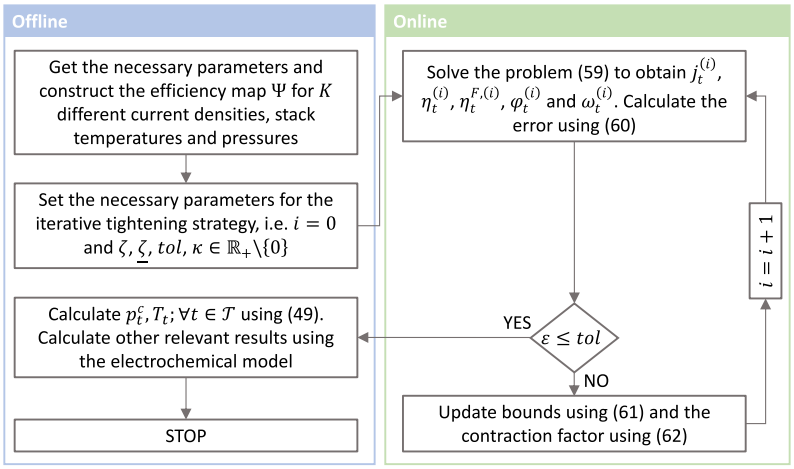

Fig. 4 – Flowchart of the developed optimization methodology.

5 – Numerical results and discussion

This section presents different case studies along with their corresponding results. To this end, the developed methodology was coded under Matlab R2021b and solved using Gurobi [52]. This solver is capable of dealing with MILP problems efficiently and offers free licenses for academic purposes. Most of the results are presented for a week-ahead time horizon with hourly resolution (168 time steps), in line with [26], but further capabilities are illustrated for year time horizons (8760 time steps). All the simulations were run on an Intel Core i7-10700K CPU 3.80GHz 3.79 GHz with 32 GB RAM.

5.1 – Input data

Table 1 collects all the parameters employed in the electrochemical model, which are mainly based on [26] and the IDAES platform [36], while the data regarding the plant described in Fig. 1 are shown in Table 2, which are mainly based on [26]. Some data that were not used in that reference (e.g., the start-up cost), were taken from [21] and scaled to the plant under consideration.

Table 1 – Parameters of the electrochemical model.

Parameter	Value	Source	Parameter	Value	Source
R	8.314 J/mol·K	[26]	δ^m	1.15	[26]
α	0.51	[26]	$a^{\mathrm{H_2O}}$	1	[26]
z	2	[25]	S	398,750 cm²	[26]
F	96,585 C/mol	[26]	Υ	2 Pa·cm²/A	[26]
j_0^{ref}	$8{\cdot}10^{-6}$ A/cm²	[26]	N	5	[26]
E_A	40,000 J/mol	[26]	γ	1.4	[31]
T^{ref}	353.15 K	[26]	η^C	0.9	[26]
R_0	$27{\cdot}10^{-3}$ Ω·cm²	[26]	T_n^{cooler}	313.15 K	[36]
d^m	51 μm	[26]	$\mathrm{LHV}^{\mathrm{H_2O}}$	241,800 J/mol	[36]

Table 2 – Parameters of the plant.

Parameter	Value	Source
$\overline{p}^G$	1.5 MW	Self-tuned
$\overline{j}$	0.2, 2 A/cm²	[26]
$\underline{j}$	0.2 A/cm²	[21]
P^{sb}	0.015 MW	[21]
PV size	2.5 MW	[26]
$\underline{H}$ / $\overline{H}$	55 / 500 kg	[26]
$\overline{m}^{in}$ / $\overline{m}^{out}$	150 / 150 kg/h	[26]
D_t	15 kg (constant)	[26]
c^{su}	193 €	[21]

PV generation depends on weather parameters such as solar irradiance and temperature. By utilizing an appropriate PV panel model (e.g., [53]), such parameters can be converted into relative power output. In line with [26], weather data from Hamburg, Germany, in 2023 were considered [54]. Electricity purchase prices were based on market electricity prices in Germany for the year 2023 [55], whereas sale rates were derived from applying additional taxes and charges [26]. For week-ahead simulations, 7 typical days were selected, which are plotted in Fig. 7 for the sake of self-sufficiency. For the McCormick tightening strategy, the parameters were tuned as follows: $\zeta = 0.2$, $\kappa = 0.01$, $\underline{\zeta} = 0.01$ and $tol = 10^{-3}$.

5.2 – Validation

The left plot of Fig. 5 presents the system and Faraday efficiencies for two operational strategies. The Reference case assumes a constant stack temperature of 80 °C and a cathode pressure of 30 bar, whereas the pTopt case optimally adjusts the temperature and pressure to maximize the system efficiency. As observed, both the system and Faraday efficiencies are significantly higher in the pTopt case at low current densities. In the Reference case, the maximum system efficiency is achieved at 1.5 A/cm², reaching ~74%, while efficiencies of up to ~82% are attained under the pTopt strategy. In both scenarios, the system efficiency decreases at current densities greater than 1.5 A/cm², stabilizing at similar values at the nominal current density (72 and 72.5% in the reference and pTopt cases, respectively). Regarding the Faraday efficiency, it increases with the current density in the Reference case, while the pTopt strategy maintains it near 99% for all the valid range of current densities.

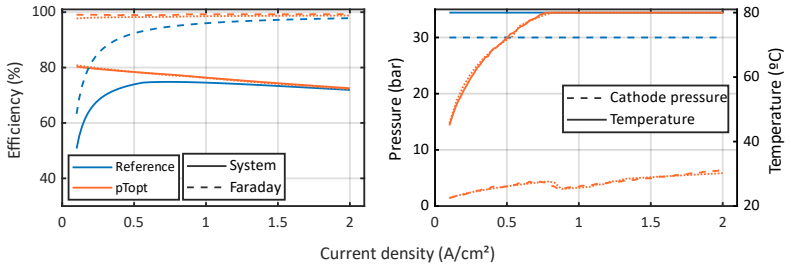

Fig. 5 – System and Faraday efficiencies (*left*) and stack temperature and cathode pressure (*right*), under reference and pTopt operational strategies. Dotted lines show results from [26] implementing the pTopt strategy.

In the right plot of Fig. 5, the stack temperature and cathode pressure are represented for different current densities. While these two parameters remain at their reference values across the entire range of current densities in the Reference case, the pTopt strategy adjusts them dynamically to maximize system efficiency. Remarkably, the cathode pressure is set significantly lower in the pTopt case, reaching a maximum value of 6.4 bar at 2 A/cm². This supports the findings in [26, 34], as operating at lower pressures reduces the backward diffusion effect, thereby compensating for the increased work required by the compressor, as discussed further later on. Similarly, lower temperatures are selected at low current densities, where the gas crossover mechanism predominates. Beyond approximately 0.8 A/cm², the maximum stack temperature is selected to maintain the cell voltage above the thermobalanced value, thus reducing the need for external heating. It is noteworthy that the results in Fig. 5 align closely with those in [26] (plotted as dotted lines), thus validating our model and maximum efficiency mapping strategy.

On the other hand, Fig. 6 compares the values of φ and ω, with their corresponding exact values, in order to validate the proposed McCormick tightening strategy. As seen, in both cases the approximated value matches almost perfectly with the exact ones, thus validating the proposed linearization strategy.

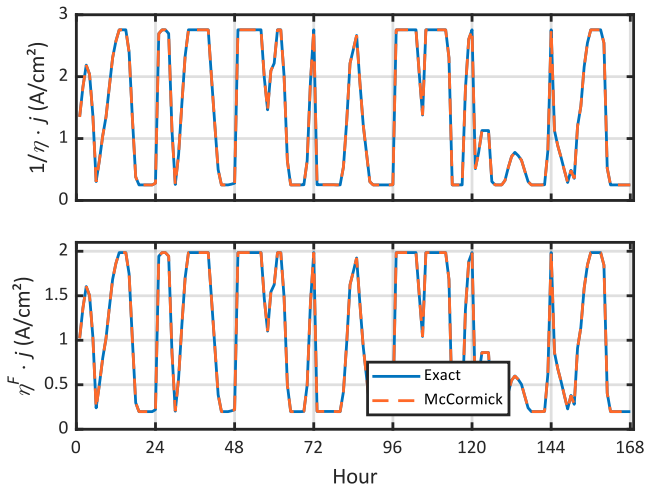

Fig. 6 – Comparison of the real values of j/η and $j\eta^F$ with their linear variables φ and ω, respectively.

5.3 – Scheduling results

Fig. 7 shows the scheduling result for both the Reference and pTopt strategies. As expected, the electrolyzer is primarily scheduled during periods of high PV production or low purchase prices. For instance, the electrolyzer operates at its maximum power at periods 30–44 h and 95–105 h, coinciding with periods of high PV production and low prices, respectively. In the first case, high PV generation reduces the need to import energy from the grid, whereas in the second case, energy is directly imported from the grid at low prices. In the Reference case, the electrolyzer is required to consume more power during less favorable hours, such as between

hours 130 and 142, when energy prices are high, while other favorable periods cannot be further leveraged (e.g., hours 48–65). It is noteworthy that the plant is capable of exporting energy during periods of high PV potential.

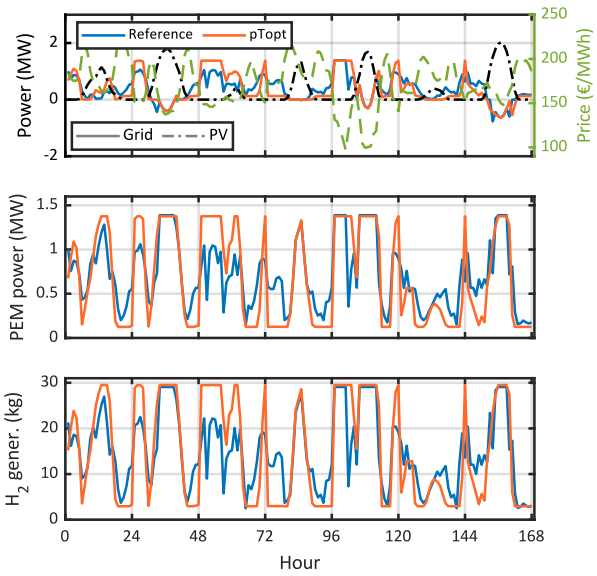

Fig. 7 – Scheduling results (*top*), electrolyzer power (*middle*) and hydrogen generated (*bottom*). Negative power indicates exports.

Fig. 8 compares the hourly system and Faraday efficiencies. In the Reference case, both system and Faraday efficiencies notably decrease when the electrolyzer works at low current densities. By contrast, optimal control of pressure and temperature allows the system to maintain high efficiency, even at very low current densities. When the electrolyzer is operated at nominal power, the efficiency in both cases is similar, although the efficiency remains higher in the pTopt case. A similar trend is observed for the Faraday efficiency. In this case, controlling pressure and temperature contributes to minimizing the gas crossover effect at low current densities, when this phenomenon is more pronounced. This explains why the Faraday efficiency remains near 99% in the pTopt case, but decreases sharply at low current densities in the Reference case.

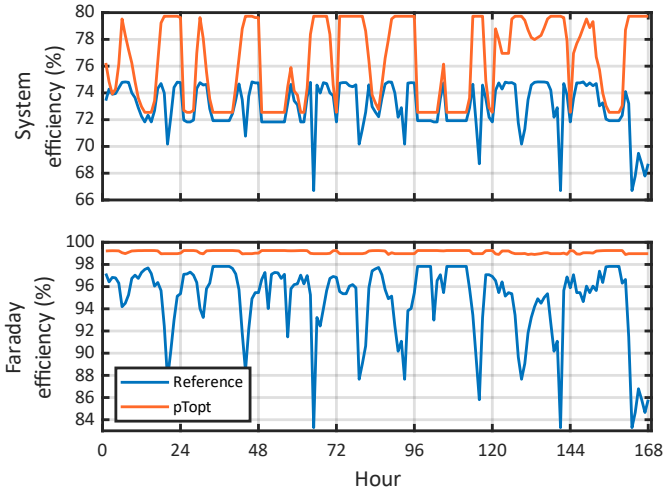

Fig. 8 – Comparison of the system (*top*) and Faraday (*bottom*) efficiencies for both the Reference and pTopt operational strategies.

Table 3 summarizes key economic and energy results. Compared to the pTopt case, the Reference case leads to a 7.3% higher import and a 2.9% higher export of energy, resulting in a 7.7% increase in net load. From an economic point of view, the plant incurs a 12.1% higher cost

in the Reference case but receives 3.8% more for energy exports. In the end, the total operating cost is 12.5% higher in the Reference case, mostly because the plant needs to import more energy to meet local demand, as it often operates at low efficiency. These results are especially relevant for assessing the economic viability of installing a temperature-pressure control system that enables the implementation of the pTopt strategy.

Table 3 – Comparison of the key economic and energy results.

Result	Reference	pTopt
Imported energy (MWh)	67.5	62.6
Exported energy (MWh)	6.8	6.6
Net load (MWh)	**60.7**	**56**
Importing cost (€)	10,902	9578.7
Exporting income (€)	503.1	484.2
Total cost (€)	**10,398.9**	**9094.5**

5.4 – Pressure and temperature

The stack temperature and working cathode pressure are analyzed in Fig. 9, together with the current density. When the electrolyzer operates at relatively high current densities (> 1.5 A/cm²), both the temperature and pressure increase in order to elevate the cell voltage while reducing compression work. Nonetheless, it is worth noting that pressure remains significantly lower in the pTopt case, with a maximum of 6.4 bar, to reduce compression consumption at high current densities. Conversely, the gas crossover effect becomes more dominant at low current densities and the pTopt strategy responds by decreasing the temperature and pressure, with minimum values of 55 °C and 2.2 bar. In the pTopt case, the maximum temperature accounts for 52% of the time horizon, with an average temperature of 70.4 °C, while the maximum pressure (30 bar) is never reached and the PEM operates at 4 bar on average. These results align perfectly with the conclusions drawn from Fig. 5, further confirming that the developed methodology effectively adjusts temperature and pressure to achieve high system efficiency.

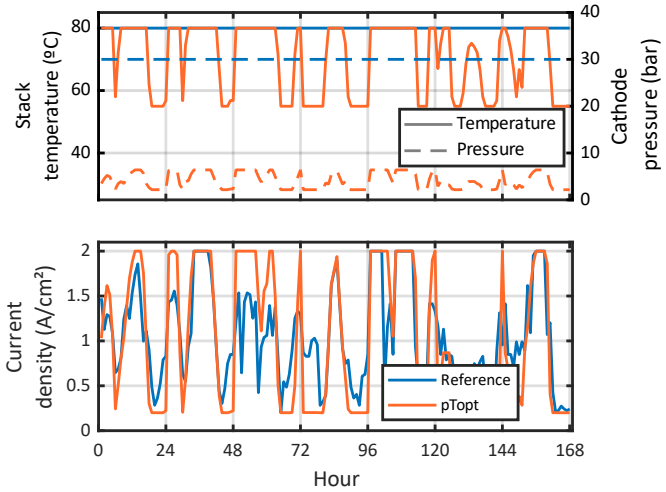

Fig. 9 – Comparison of the temperature and pressure (*top*), and current density (*bottom*) for both the Reference and pTopt operational strategies.

5.5 – Gas crossover

Gas crossover is an important mechanism in PEM electrolyzers, by which hydrogen and oxygen permeate through the membrane. A key measure of the gas crossover phenomenon is the anodic hydrogen content (AHC), which is calculated as follows:

$$\mathrm{AHC} = \frac{\dot{n}_d^{H_2,v}}{\dot{n}^{O_2,v} + \dot{n}_d^{H_2,v}} \cdot 100 \tag{63}$$

In addition to reducing the amount of usable hydrogen, the gas crossover effect may pose an explosion risk if the AHC exceeds a threshold of 4% [56]. Fig. 10 compares the AHC for both the Reference and pTopt strategies. As illustrated, the Reference case consistently shows a significantly higher AHC, often reaching very high values near 27%. In the Reference case, the AHC is inversely proportional to the current density. Indeed, at low current densities, the amount of oxygen produced is relatively low compared to the hydrogen that permeates through the membrane. In contrast, the pTopt strategy enables optimal adjustment of pressure and temperature, effectively reducing the gas crossover effect even at low current densities. Notably, when the pTopt strategy is implemented, the AHC remains below 4%.

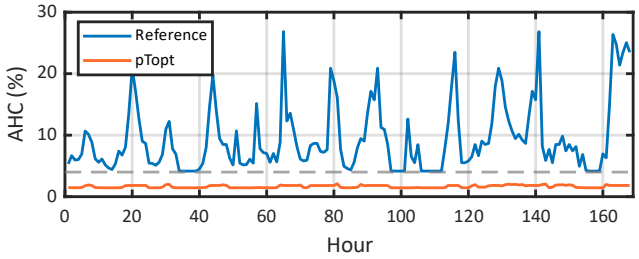

Fig. 10 – Comparison of the AHC for both the Reference and pTopt operational strategies.

5.6 – Sensitivity analysis

5.6.1 – System-level parameters

Additional results are presented in this section to evaluate the influence of various input parameters on the overall system performance. Fig. 11 illustrates a comparison of system efficiency as a function of membrane thickness and current density. In the Reference scenario, thin membranes exacerbate gas crossover effect at low current densities, resulting in a very low efficiency. This negative effect is better controlled when implementing a pTopt strategy by optimally adjusting the working pressure. By contrast, when working at high current densities, membrane thickness has a negative effect on efficiency, due to an increment on the ohmic overvoltage.

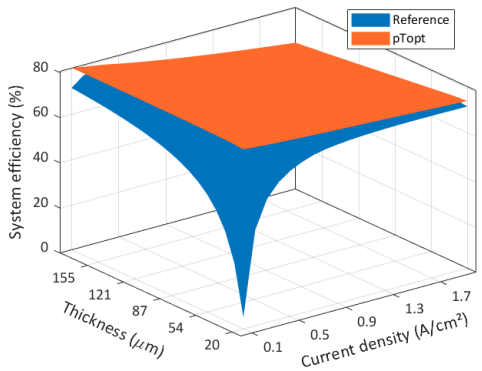

Fig. 11 – Comparison of system efficiency for different membrane thicknesses and current densities

Fig. 12 presents results analogous to those shown in Fig. 11. However, in this case, system efficiency is analyzed as a function of varying compressor efficiencies. The impact of compressor efficiency on overall system performance is found to be marginal, primarily because the energy consumption associated with compression is relatively low compared to other energy balances. Nevertheless, its influence is more pronounced in the Reference case, where the absence of optimized cathode pressure control leads to a greater sensitivity to low compressor efficiencies.

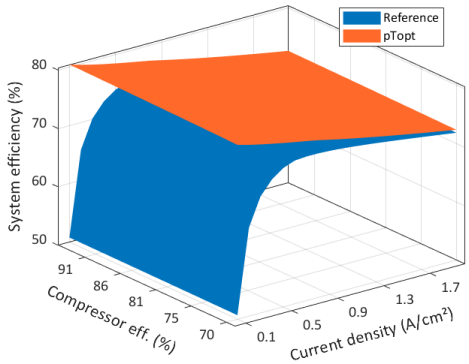

Fig. 12 – Comparison of system efficiency for different compressor efficiencies and current densities

5.6.2 – Plant-level parameters

Fig. 13 illustrates the impact of varying PV array sizes on system performance. As expected, increasing PV capacity reduces total operational costs by enhancing self-sufficiency and enabling greater energy exports. Notably, when using a 5 MW PV array, total costs decrease by up to 38% with the implementation of the pTopt strategy. These results highlight that the economic benefits of the proposed strategy grow with PV size, reflecting its ability to better exploit locally generated renewable energy. Energy imports decline as PV capacity increases, following a trend closely aligned with total cost. This correlation is consistent, given that imported electricity constitutes the main component of operational expenses. By contrast, energy exports rise with PV size but remain similar across both strategies. However, the revenue generated from exports is significantly lower than the cost of imports, underscoring the importance of minimizing reliance on grid electricity to improve economic performance.

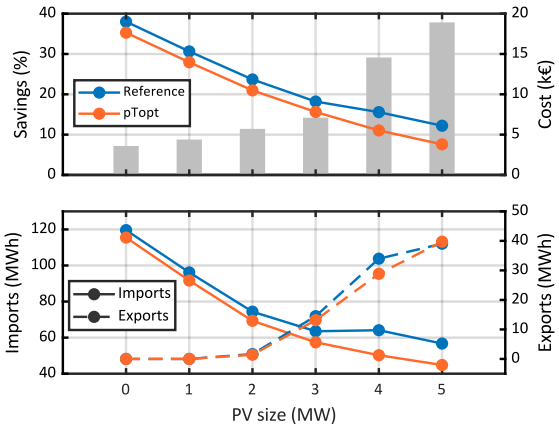

Fig. 13 – Total cost (*top*) and energy imports/exports (*bottom*) for different PV sizes. Monetary savings when adopting a pTopt strategy are shown in gray bars.

Fig. 14 presents results analogous to those in Fig. 13, comparing both operational strategies under varying weekly hydrogen demands. As expected, when demand is zero, total costs are identical for both strategies, since the electrolyzer remains idle and the plant solely exports PV-generated electricity. This results in a revenue of approximately 4.8k€, with no associated production costs. As hydrogen demand increases, more grid energy must be imported, leading to higher operational costs. Nonetheless, the plant remains economically viable at moderate demand levels. For instance, at 840 kg/week, the pTopt strategy still enables a net revenue, illustrating its effectiveness in managing energy use. Total costs are consistently higher under the Reference strategy. However, the relative advantage of pTopt diminishes with increasing demand. At 4200 kg/week, cost savings decrease to about 4.5%, as the electrolyzer operates more frequently near

its maximum current density, where efficiency differences between strategies are less significant. These results confirm that the pTopt strategy provides economic benefits, particularly at low to moderate demand levels, while maintaining robust performance even as demand increases.

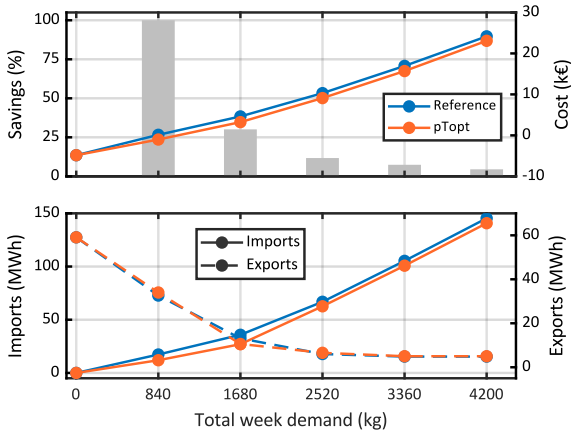

Fig. 14 – Total cost (*top*) and energy imports/exports (*bottom*) for different week demands. Monetary savings when adopting a pTopt strategy are shown in gray bars.

5.7 – Comparison with nonlinear models

To further highlight the advantages of the developed model and demonstrate the merits of the MILP optimization formulation over nonlinear approaches, the overall performance of the proposed method was compared with two well-established nonlinear solvers. It is important to note that, in order to keep the problem solvable without relying on advanced optimization techniques, binary variables were excluded from the nonlinear formulations.

The first solver used in the comparison was 'fmincon', the standard nonlinear solver in Matlab R2021b. In this case, the electrochemical model was explicitly included, fully accounting for the nonlinear relationships between temperature, pressure, and current density. However, the solver terminated prematurely without reaching the default optimality tolerance within a reasonable timeframe, which was set to 400 iterations (~1 hour in our experimental setup).

Given the computational challenges encountered with 'fmincon' for large-scale nonlinear models, the same problem was subsequently solved using IPOPT [57] in Python. This approach yielded satisfactory results within approximately 600 seconds. By contrast, our MILP-based approach was able to solve the same model, including binary variables, in just 30–35 seconds.

This significant computational efficiency offers multiple advantages, particularly in terms of scalability, as further illustrated in the subsequent section. Additionally, the fast computation time makes the developed tool suitable for real-time or short-term applications, where rapid results are crucial. Furthermore, the computational superiority of our approach facilitates its use in sensitivity analysis, enabling the evaluation of various solutions within a reasonable timeframe.

5.8 – Scalability

The results discussed above demonstrate the performance of the proposed control strategy in the baseline configuration of a 1.5 MW electrolysis system. To evaluate the scalability of the approach, this section presents simulation results for a large-scale system. Currently, the largest operational PEM electrolyzer installations worldwide reach a rated power of 20 MW, such as those located in Bécancour, Canada and Puertollano, Spain [58,59]. Accordingly, to assess the performance of the proposed methodology under similar conditions, the parameters used in previous simulations were scaled up to a nominal power of 20 MW. This approach was adopted due to the lack of publicly available data on specific characteristics of these commercial installations, such as total active cell area. Nevertheless, this assumption is justified by the modular nature of PEM electrolyzers, which enables high power outputs through the aggregation of smaller units. For instance, the Bécancour facility comprises four PEM stacks of 5 MW each,

while the Puertollano plant consists of sixteen 1.25 MW stacks. Under the 20 MW assumption, implementation of the pTopt control strategy allows reducing the total cost from 138,590€ to 121,280€, with computational time remaining comparable to that of the baseline case. Fig. 15 summarizes the results from the scalability analysis, which are consistent with those from previous simulations, thereby confirming that the proposed control strategy maintains robust performance with increasing system size.

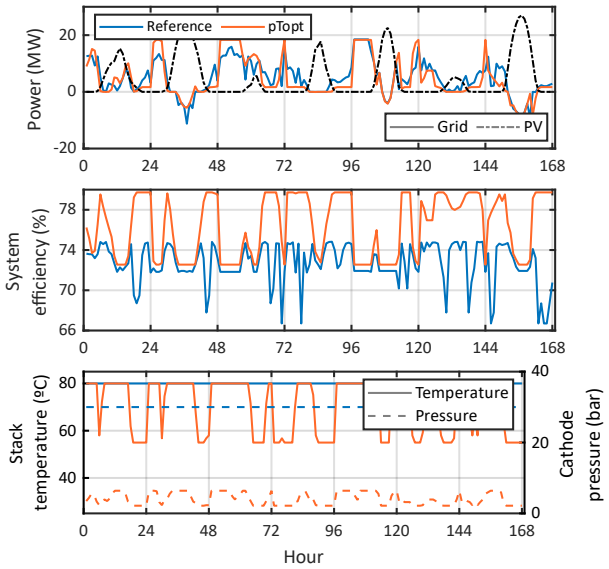

Fig. 15 – Scheduling results (*top*), system efficiency (*middle*), and temperature/pressure (*bottom*) obtained in a 20 MW plant. Negative power indicates exports.

The new proposal solves a series of MILP problems, which can be efficiently handled using off-the-shelf solvers. This represents a major advantage of the proposed methodology over other computational tools such as in [26]. Indeed, the computational time typically ranges from 15 to 30 seconds, on average, which is more than reasonable for a week-ahead scheduling tool. Promising results suggest that the developed tool can be applied to longer time horizons. To verify this, the proposed methodology was executed on a one-year time period with hourly resolution (8760 time steps), using the same data as in the week-ahead case (sales rates were taken at 40% than imports ones), but without relying on time series aggregation techniques. In this scenario, the resolution time was in the order of 30 minutes, which is acceptable when dealing with yearly time horizons, as typically in planning tools that are executed offline [60].

Considering data over an entire year offers several important advantages. Most notably, it enables a more accurate assessment of hydrogen storage system performance by effectively capturing both intraday variations and long-term seasonal trends [61]. These aspects are particularly relevant when evaluating the economic viability of hydrogen-based storage technologies, which (unlike other energy storage systems [62]) are strongly influenced by seasonal dynamics over extended time horizons.

To illustrate this aspect, Fig. 16 presents the total hydrogen stored during two representative months: August and December. Using full-year data, as opposed to focusing on a single week, allows for a more comprehensive representation of both intraday and seasonal storage patterns. This approach provides a more accurate evaluation of the hydrogen storage system's viability and scheduling, as it captures variations over longer timeframes. Intraday trends clearly exhibit a charging pattern in the morning, when PV generation increases, followed by discharging during the evening and night hours. Seasonally, the storage system is more fully charged in August, benefiting from the higher solar energy production during summer months. Moreover, the total cost analysis demonstrates a 15% reduction in costs when implementing the pTopt strategy, highlighting its efficiency in optimizing both energy use and hydrogen storage over time.

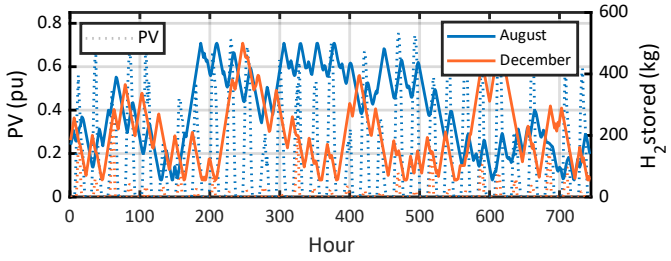

Fig. 16 – Total hydrogen stored in August and December using a pTopt strategy.

5.9 – Discussion

The results presented in this paper further validate the conclusions drawn in previous studies, such as [25, 26]. Indeed, optimal adjustments of cathode pressure and stack temperature ensure that PEM electrolyzers operate with high efficiency across the entire valid range of operational current densities. In general, low temperatures and pressures are preferred at low current densities, where the gas crossover effect predominates and significantly impacts system performance. As the current density increases, both temperature and pressure should be progressively elevated to reduce the thermal and compression energy demands. Nevertheless, operational pressure remains significantly lower compared to the Reference case, in order to mitigate the gas crossover effect when operating at high current densities. The negative effects associated with gas crossover can be further diminished by increasing the membrane thickness, which acts as a diffusion barrier. However, implementing a pTopt strategy enables effective control of the gas crossover phenomenon through cathode pressure optimization, even when using thinner membranes, thereby enhancing overall system efficiency without compromising material or design constraints.

Although optimally adjusting temperature and pressures offers multiple safety and economic advantages, prolonged dynamic operation under such variable conditions may accelerate degradation mechanisms, especially in the anode catalyst layer (ACL), where transport and reaction processes fluctuate rapidly. In this regard, ref. [63] introduces a temporal multiscale modeling approach that simulates these degradation processes by decoupling fast-scale transport-reaction dynamics from slow-scale material degradation. Their study demonstrates that dynamic operation influences catalyst dissolution and provides a pathway for integrating performance and durability modeling. Furthermore, ref. [64] investigates the effects of dynamic, fluctuating power inputs on PEM electrolyzers, with a particular focus on the accelerated degradation of the ACL during high-frequency switching, such as the operation of wind-powered systems. Their findings show that dynamic operation under conditions that involve rapid voltage changes between open circuit voltage (OCV) and operational states, or frequent transitions between high and low current densities, especially in cells with low anode catalyst loading, leads to increased degradation rates. However, if periods of OCV and sudden fluctuations between high and low current densities or cell voltages are avoided, dynamic operation can benefit the longevity of PEM water electrolyzers [65, 66]. Although a further analysis on electrolyzer degradation is out of the scope of this paper, future work should build on these modeling approaches to comprehensively evaluate the trade-offs between operational efficiency and component longevity in the context of dynamic operation of PEM water electrolyzers.

It has been demonstrated that the AHC remains at risky levels when relying on a conventional operational strategy, particularly at low current densities, where the permeation of hydrogen towards the anode is more pronounced. This situation can be mitigated by reducing the operational temperature and pressure, thereby decreasing the relative concentration of hydrogen at the anode and minimizing safety risks. From an economic perspective, the implementation of the pTopt strategy can lead to considerable cost reductions, with potential savings of up to 38%, mainly due to improved efficiency. However, in scenarios where the electrolyzer is frequently operated near its maximum current density (where thermal and mass transport limitations dominate) the

performance gap between the pTopt and conventional strategies narrows. In such cases, the added complexity and cost of implementing a control system for real-time dynamic adjustment of pressure and temperature may not be economically justified, and a simplified strategy could be more suitable depending on the operational profile and investment constraints.

Economic outcomes can be more accurately assessed over extended time horizons (such as an entire year) where seasonal fluctuations and long-term operational patterns of hydrogen storage systems can be more thoroughly captured. Results derived from full-year datasets highlight that evaluating hydrogen storage performance over short periods (e.g., daily or weekly) may lead to misleading conclusions, as they fail to reflect the cumulative and cyclical behavior of energy systems. In this context, the developed optimization tool demonstrates a strong capability to efficiently manage large temporal datasets, thereby providing a robust framework for the comprehensive evaluation of water electrolysis installations under realistic operating conditions. Furthermore, the scalability of the proposed approach has been validated through its application to a 20 MW plant, where it delivered reliable and consistent results within competitive computation times, reinforcing its practical relevance for industrial-scale implementations.

6 – Conclusion

A new optimization methodology for optimally adjusting pressure and temperature in PEM electrolyzers has been presented in this paper. The proposed approach evaluates the maximum system efficiency for different current densities and incorporates this map into the optimization model. Nonlinearities are addressed through the application of a tightening McCormick algorithm. The final optimization problem is cast as a solvable MILP model, which can be efficiently solved using off-the-shelf solvers. Furthermore, this formulation also allows for the inclusion of binary variables, enabling a precise representation of the electrolyzer operational states.

After extensive testing in different case studies, the results of the new proposal lead to the following conclusions:

- Significant cost savings can be achieved through optimal control of temperature and pressure, particularly when the electrolyzer operates frequently at low current densities. Specifically, the pTopt control strategy allows reducing costs by 12.5% over a week horizon in the case study.
- In contrast to conventional strategies, lower temperatures and pressures are preferable under partial load conditions, primarily due to the dominance of gas crossover effects in this regime.
- Implementing an optimal temperature-pressure control strategy allows leveraging further local renewable generation, especially due to the typical operation at a higher level of efficiency.
- The economic benefits of dynamic control diminish as hydrogen demand increases and the electrolyzer operates closer to its rated capacity. Under these conditions, the efficiency achieved with dynamic control closely resembles that of conventional strategies, making the advantage of temperature–pressure optimization less pronounced.
- Dynamic control of operating conditions contributes to reducing the anodic hydrogen content, thereby enhancing the safety of the electrolyzer during operation.
- The proposed model demonstrates a significant improvement in computational performance compared to conventional nonlinear models, exhibiting a considerably lower computational burden in comparison with ‘fmincon’ and IPOPT.
- The MILP-based formulation provides significant scalability advantages over previous nonlinear approaches, enabling application to large-scale systems and extended time horizons (e.g., one year). This facilitates a more accurate representation of seasonal hydrogen storage dynamics and long-term system behavior.

Optimally controlling pressure and temperature can be highly beneficial in isolated installations, where electrolyzers must adapt to variable renewable generation and often operate under partial load conditions. Future research should focus on further exploring this aspect, specifically examining the trade-off between utilization factor and the economic viability of a control system that enables dynamic regulation of operating conditions. Moreover, the effect of dynamic control on electrolyzer degradation requires a more comprehensive analysis. In this context, the developed model could serve as a valuable tool for evaluation, as it can be easily implemented in different software platforms and programming languages.

CRediT authorship contribution statement

Roque Aguado: Methodology, Software, Validation, Formal analysis, Data curation, Writing - Original Draft, Writing - Review & Editing. **Marcos Tostado-Véliz**: Conceptualization, Methodology, Software, Formal analysis, Investigation, Writing - Original Draft, Writing - Review & Editing. **Umberto Desideri**: Resources, Visualization, Supervision, Project administration. **Francisco Jurado**: Resources, Visualization, Project administration.

Acknowledgments

Marcos Tostado-Véliz thanks the Department of Energy, Systems, Territory and Building Engineering at the University of Pisa for hosting his research stay, during which this work was conceptualized.

Declaration of generative AI and AI-assisted technologies in the writing process

During the preparation of this work the authors used Chatgpt in order to polish the use of English. After using this tool, the authors reviewed and edited the content as needed and take full responsibility for the content of the published article.

References

[1] IPCC. Climate Change 2007: Synthesis Report. Contribution of Working Groups I, II and III to the Fourth Assessment Report of the Intergovernmental Panel on Climate Change. Pachauri RK, Reisinger A, editors. IPCC, Geneva, Switzerland, 2007.

[2] IRENA. Hydrogen: A renewable energy perspective, 2019. https://www.irena.org/publications/2019/Sep/Hydrogen-A-renewable-energy-perspective (accessed 5 March 2025).

[3] European Commission. Renewable Hydrogen. https://energy.ec.europa.eu/topics/eus-energy-system/hydrogen/renewable-hydrogen_en (accessed 5 March 2025).

[4] IEA. Global Hydrogen Review 2024. IEA, Paris, 2024. https://www.iea.org/reports/global-hydrogen-review-2024 (accessed 5 March 2025).

[5] Götz M, et al. Renewable Power-to-Gas: A technological and economic review. Renew Energy 2016;85:1371-90. https://doi.org/10.1016/j.renene.2015.07.066.

[6] Schmidt O, Gambhir A, Staffel I, Hawkes A, Nelson J, Few S. Future cost and performance of water electrolysis: An expert elicitation study. Int J Hydrogen Energy 2017;42(52):30470-92. https://doi.org/10.1016/j.ijhydene.2017.10.045.

[7] Carmo M, Fritz DL, Mergel J, Stolten D. A comprehensive review on PEM water electrolysis. Int J Hydrogen Energy 2013;38(12):4901-34. https://doi.org/10.1016/j.ijhydene.2013.01.151.

[8] IRENA. Green Hydrogen Cost Reduction: Scaling up Electrolysers to Meet the 1.5ºC Climate Goal. IRENA, Abu Dhabi, 2020. https://www.irena.org, (accessed 5 Mar. 2025).

[9] Varcoe JR, Šulc P, Tabares J, Owen J, Rand D. Anion-exchange membranes in electrochemical energy systems. Energy Environ Sci 2014;7:3135-91. https://doi.org/10.1039/C4EE01303D.

[10] Hino R, Haga K, Aita H, Sekita K. R&D on hydrogen production by high-temperature electrolysis of steam. Nucl Eng Des 2004;233(1-3):363-75. https://doi.org/10.1016/j.nucengdes.2004.08.029.

[11] El-Shafie M. Hydrogen production by water electrolysis technologies: A review. Results Eng 2023;20:101426. https://doi.org/10.1016/j.rineng.2023.101426.

[12] Tostado-Véliz M, Horrillo-Quintero P, García-Triviño P, Fernández-Ramírez LM, Jurado F. Optimal sitting and sizing of hydrogen refilling stations in distribution networks under locational marginal prices, Appl Energy 2024;374:124075. https://doi.org/10.1016/j.apenergy.2024.124075.

[13] Tostado-Véliz M, Arévalo P, Jurado F. A comprehensive electrical-gas-hydrogen microgrid model for energy management applications. Energy Convers Manag 2021;228:113726. https://doi.org/10.1016/j.enconman.2020.113726.

[14] Zeng Y, Wang Y, Chen H, Zhang Y. Scheduling multiple industrial electrolyzers in renewable P2H systems: A coordinated active-reactive power management method. IEEE Trans Sustain Energy 2025;16(1):201-15. https://doi.org/10.1109/TSTE.2024.3450503.

[15] Tostado-Véliz M, Jordehi AR, Fernández-Lobato L, Jurado F. Robust energy management in isolated microgrids with hydrogen storage and demand response. Appl Energy 2023;345:121319. https://doi.org/10.1016/j.apenergy.2023.121319.

[16] Feng W, Ruiz C. Risk management of energy communities with hydrogen production and storage technologies. Appl Energy 2023;348:121494. https://doi.org/10.1016/j.apenergy.2023.121494.

[17] Matute G, Yusta JM, Correas LC. Techno-economic modelling of water electrolyzers in the range of several MW to provide grid services while generating hydrogen for different applications: A case study in Spain applied to mobility with FCEVs. Int J Hydrogen Energy 2019;44(33):17431-42. https://doi.org/10.1016/j.ijhydene.2019.05.092.

[18] Tostado-Véliz M, Jordehi AR, Mansouri SA, Escámez A, Alharthi YZ, Jurado F. Risk-averse electrolyzer sizing in industrial parks: An efficient stochastic-robust approach. Appl Energy 2024;367:123389. https://doi.org/10.1016/j.apenergy.2024.123389.

[19] Varela C, Mostafa M, Zondervan E. Modeling alkaline water electrolysis for power-to-x applications: A scheduling approach. Int J Hydrogen Energy 2021;46(14):9303-13. https://doi.org/10.1016/j.ijhydene.2020.12.111.

[20] Pavić I, Čović N, Pandžić H. PV-battery-hydrogen plant: Cutting green hydrogen costs through multi-market positioning. Appl Energy 2022;328:120103. https://doi.org/10.1016/j.apenergy.2022.120103.

[21] Baumhof MT, Raheli E, Johnsen AG, Kazempour J. Optimization of Hybrid Power Plants: When is a Detailed Electrolyzer Model Necessary?. 2023 IEEE Belgrade PowerTech, Belgrade, Serbia, 2023. https://doi.org/10.1109/PowerTech55446.2023.10202860.

[22] Raheli E, Werner Y, Kazempour J. A conic model for electrolyzer scheduling. Comput Chem Eng 2023;179: 108450. https://doi.org/10.1016/j.compchemeng.2023.108450.

[23] Niu X, Ma N, Bu Z, Hong W, Li H. Thermodynamic analysis of supercritical Brayton cycles using CO2-based binary mixtures for solar power tower system application. Energy 2022;254(A):124286. https://doi.org/10.1016/j.energy.2022.124286.

[24] Buttler A, Spliethoff H. Current status of water electrolysis for energy storage, grid balancing and sector coupling via power-to-gas and power-to-liquids: A review. Renew Sustainable Energy Rev 2018;82(3):2440-54. https://doi.org/10.1016/j.rser.2017.09.003.

[25] Schalenbach M, Tjarks G, Carmo M, Lueke W, Mueller M, Stolten D. Acidic or Alkaline? Towards a New Perspective on the Efficiency of Water Electrolysis. J Electrochem Soc 2016;163:F3197. https://doi.org/10.1149/2.0271611jes.

[26] Bornemann L, Lange J, Kaltschmitt M. Optimizing temperature and pressure in PEM electrolyzers: A model-based approach to enhanced efficiency in integrated energy systems. Energy Convers Manag 2025;325:119338. https://doi.org/10.1016/j.enconman.2024.119338.

[27] Bonanno M, et al. Review and Prospects of PEM Water Electrolysis at Elevated Temperature Operation. Adv Mater Technol 2023;9(2):2300281. https://doi.org/10.1002/admt.202300281.

[28] Gabrielli P, Flamm B, Eichler A, Gazzani M, Lygeros J, Mazzotti M. Modeling for optimal operation of PEM fuel cells and electrolyzers. 2016 IEEE 16th International Conference on

Environment and Electrical Engineering (EEEIC), Florence, Italy, 2016. https://doi.org/10.1109/EEEIC.2016.7555707.

[29] Gabrielli P, Gazzani M, Mazzotti M. Electrochemical conversion technologies for optimal design of decentralized multi-energy systems: Modeling framework and technology assessment. Appl Energy 2018;221: 557-75. https://doi.org/10.1016/j.apenergy.2018.03.149.

[30] Li J, Lin J, Song Y, Xing X, Fu C. Operation Optimization of Power to Hydrogen and Heat (P2HH) in ADN Coordinated With the District Heating Network. IEEE Trans Sustainable Energy 2019;10(4):1672-83. https://doi.org/10.1109/TSTE.2018.2868827.

[31] Zheng Y, You S, Bindner HW, Münster M. Optimal day-ahead dispatch of an alkaline electrolyzer system concerning thermal–electric properties and state-transitional dynamics. Appl Energy 2022;307:118091. https://doi.org/10.1016/j.apenergy.2021.118091.

[32] Baader FJ, Bardow A, Dahmen M. MILP Formulation for Dynamic Demand Response of Electrolyzers. Comput Aided Chem Eng 2022;49:391–396. https://doi.org/10.1016/B978-0-323-85159-6.50065-8.

[33] Valverde L, Rosa F, del Real AJ, Arce A, Bordons C. Modeling, simulation and experimental set-up of a renewable hydrogen-based domestic microgrid Int J Hydrogen Energy 2013;38(27):11672-84. https://doi.org/10.1016/j.ijhydene.2013.06.113.

[34] Hancke R, Bujlo P, Holm T, Ulleberg Ø. High-pressure PEM water electrolyzer performance up to 180 bar differential pressure. J Power Sources 2024;601:234271. https://doi.org/10.1016/j.jpowsour.2024.234271.

[35] Molina-Pérez D, Mezura-Montes E, Portilla-Flores EA, Vega-Alvarado E, Calva-Yañez B. A differential evolution algorithm for solving mixed-integer nonlinear programming problems. Swarm Evol Comput 2024;84:101427. https://doi.org/10.1016/j.swevo.2023.101427.

[36] Lee A, et al. The IDAES process modeling framework and model library-Flexibility for process simulation and optimization. J Adv Manuf Process 2021;3(3):e10095. https://doi.org/10.1002/amp2.10095.

[37] NIST Chemistry WebBook. https://webbook.nist.gov/chemistry/, (accessed 5 Mar. 2025).

[38] Green DW, Perry RH. Perry's Chemical Engineers' Handbook. New York: McGraw-Hill; 2007. ISBN 9780071422949.

[39] Scheepers F, et al. Temperature optimization for improving polymer electrolyte membrane-water electrolysis system efficiency. Appl Energy 2021;283:116270. https://doi.org/10.1016/j.apenergy.2020.116270.

[40] Schalenbach M, Hoefner T, Paciok P, Carmo M, Lueke W, Stolten D. Gas Permeation through Nafion. Part 1: Measurements. J Phys Chem C 2015;119(45):25145-55. https://doi.org/10.1021/acs.jpcc.5b04155.

[41] Tostado-Véliz M, Hasanien HM, Carpio J, Jurado F. Risk-aware strategies for optimal participation of parking lots in day-ahead electricity markets. Energy 2025;322:135406 https://doi.org/10.1016/j.energy.2025.135406.

[42] Javadi MS, Lotfi M, Nezhad AE, Anvari-Moghaddam A, Guerrero JM, Catalão JPS. Optimal operation of energy hubs considering uncertainties and different time resolutions. IEEE Trans Ind Appl 2020;56(5):5543-52. https://doi.org/10.1109/TIA.2020.3000707.

[43] Roald LA, Pozo D, Papavasiliou A, Molzahn DK, Kazempour J, Conejo A. Power systems optimization under uncertainty: A review of methods and applications. Electric Power Syst Res 2023;214(A):108725. https://doi.org/10.1016/j.epsr.2022.108725.

[44] Yang M, Han C, Zhang W, Fang G, Jia Y. A short-term power prediction method based on numerical weather prediction correction and the fusion of adaptive spatiotemporal graph feature information for wind farm cluster. Expert Syst Appl 2025;274:126979. https://doi.org/10.1016/j.eswa.2025.126979.

[45] Lakouraj MM, Niaz H, Liu JJ, Siano P, Anvari-Moghaddam A. Optimal risk-constrained stochastic scheduling of microgrids with hydrogen vehicles in real-time and day-ahead markets. J Clean Prod 2021;318:128452. https://doi.org/10.1016/j.jclepro.2021.128452

[46] Kuchlbauer M. Outer approximation for generalized convex mixed-integer nonlinear robust optimization problems. Oper Res Lett 2025;60:107243. https://doi.org/10.1016/j.orl.2025.107243.

[47] Molina-Pérez D, Mezura-Montes E, Portilla-Flores EA, Vega-Alvarado E, Calva-Yañez B. Efficiently handling constraints in mixed-integer nonlinear programming problems using gradient-based repair differential evolution. PeerJ Comput Sci 2024;10:e2095. https://doi.org/10.7717/peerj-cs.2095.

[48] Wei Z, Ali MM, Xu L, Zeng B, Yao J-C. On solving nonsmooth mixed-integer nonlinear programming problems by outer approximation and generalized Benders decomposition. J Optim Theory Appl 2019;181:840-63. https://doi.org/10.1007/s10957-019-01499-7.

[49] Tomazella CP, Nagano MS. A comprehensive review of Branch-and-Bound algorithms: Guidelines and directions for further research on the flowshop scheduling problem. Expert Syst Appl 2020;158:113556. https://doi.org/10.1016/j.eswa.2020.113556.

[50] Bukhari FA, Alnowibet KA, Abdelgawad AE. Robust wind power capacity planning under fuel price uncertainty using conic duality theory and piecewise McCormick relaxation. Electric Power Syst Res 2025;238:111127. https://doi.org/10.1016/j.epsr.2024.111127.

[51] Deng L, Sun H, Li B, Sun Y, Yang T, Zhang X. Optimal Operation of Integrated Heat and Electricity Systems: A Tightening McCormick Approach, Eng 2021;7(8):1076-86. https://doi.org/10.1016/j.eng.2021.06.006.

[52] Gurobi Optimization L.L.C. Gurobi Optimizer Reference Manual. 2021. https://www.gurobi.com, (accessed 5 Mar. 2025).

[53] Tostado-Véliz M, Mouassa S, Jurado F. A MILP framework for electricity tariff-choosing decision process in smart homes considering 'Happy Hours' tariffs. Int J Electr Power Energy Syst 2021;131:107139. https://doi.org/10.1016/j.ijepes.2021.107139.

[54] Pfenninger S, Staffell I. Long-term patterns of European PV output using 30 years of validated hourly reanalysis and satellite data. Energy 2016;114:1251-65. https://doi.org/10.1016/j.energy.2016.08.060.

[55] Eurostat. Electricity prices for non-household consumers - bi-annual data (from 2007 onwards), Statistical Office of the European Union. https://ec.europa.eu/eurostat/databrowser/view/nrg_pc_205/default/table?lang=en, (accessed 5 Mar. 2025).

[56] Klose C, et al. Membrane Interlayer with Pt Recombination Particles for Reduction of the Anodic Hydrogen Content in PEM Water Electrolysis. J Electrochem Soc 2018;165:F1271. https://doi.org/10.1149/2.1241814jes.

[57] Wächter A, Biegler LT. On the implementation of an interior-point filter line-search algorithm for large-scale nonlinear programming. Math Program 2005;106:25-57. https://doi.org/10.1007/s10107-004-0559-y.

[58] Boretti A. Challenges of a "free market" approach to the hydrogen economy. Int J Hydrogen Energy 2024;83:897-902. https://doi.org/10.1016/j.ijhydene.2024.08.086.

[59] Yang J, Lam TY, Luo Z, Cheng Q, Wang G, Yao H. Renewable energy driven electrolysis of water for hydrogen production, storage, and transportation. Renew Sustain Energy Rev 2025;218:115804. https://doi.org/10.1016/j.rser.2025.115804.

[60] Tostado-Véliz M, Hasanien HM, Gómez-González M, Jurado F. Robust rooftop photovoltaic planning in energy communities. Renewable Energy 2025;243:122601. https://doi.org/10.1016/j.renene.2025.122601.

[61] Tejada-Arango DA, Domeshek M, Wogrin S, Centeno E. Enhanced Representative Days and System States Modeling for Energy Storage Investment Analysis. IEEE Trans Power Syst 2018; 33(6):6534-44. https://doi.org/10.1109/TPWRS.2018.2819578.

[62] Zhan Y, Ren X, Zhao S, Guo Z. Enhancing prediction of electron affinity and ionization energy in liquid organic electrolytes for lithium-ion batteries using machine learning. J Power Sources 2025;629:235992. https://doi.org/10.1016/j.jpowsour.2024.235992.

[63] Dominguez DC, Dam AP, Alia SM, Richter T, Sundmacher K. Application of a temporal multiscale method for efficient simulation of degradation in PEM Water Electrolysis under dynamic operating conditions. Comput Chem Eng 2025;198:109083. https://doi.org/10.1016/j.compchemeng.2025.109083.

[64] Pape S-V, et al. Performance data extraction from dynamic long-term operation of proton exchange membrane and alkaline water electrolysis cells. Int J Hydrogen Energy 2025;127:51-63. https://doi.org/10.1016/j.ijhydene.2025.03.387.

[65] Frensch SH, Fouda-Onana F, Serre G, Thoby D, Araya SS, Kær SK. Influence of the operation mode on PEM water electrolysis degradation. Int J Hydrogen Energy 2019;44(57):29889-98. https://doi.org/10.1016/j.ijhydene.2019.09.169.

[66] Alia SM, Stariha S, Borup RL. Electrolyzer Durability at Low Catalyst Loading and with Dynamic Operation. J Electrochem Soc 2019;166:F1164. https://doi.org/10.1149/2.0231915jes.